Internal Tidal Modal Ray Refraction and Energy Ducting in Baroclinic Gulf Stream Currents

TIMOTHY F. DUDA AND YING-TSONG LIN

Applied Ocean Physics and Engineering Department, Woods Hole Oceanographic Institution, Woods Hole, Massachusetts

MAARTEN BUIJSMAN

Department of Marine Science, University of Southern Mississippi, Stennis Space Center, Mississippi

ARTHUR E. NEWHALL

Applied Ocean Physics and Engineering Department, Woods Hole Oceanographic Institution, Woods Hole, Massachusetts

(Manuscript received 14 February 2018, in final form 28 June 2018)

ABSTRACT

Upstream mean semidiurnal internal tidal energy flux has been found in the Gulf Stream in hydrodynamical model simulations of the Atlantic Ocean. A major source of the energy in the simulations is the south edge of Georges Bank, where strong and resonant Gulf of Maine tidal currents are found. An explanation of the flux pattern within the Gulf Stream is that internal wave modal rays can be strongly redirected by baroclinic currents and even trapped (ducted) by current jets that feature strong velocities above the thermocline that are directed counter to the modal wavenumber vector (i.e., when the waves travel upstream). This ducting behavior is analyzed and explained here with ray-based wave propagation studies for internal wave modes with anisotropic wavenumbers, as occur in mesoscale background flow fields. Two primary analysis tools are introduced and then used to analyze the strong refraction and ducting: the generalized Jones equation governing modal properties and ray equations that are suitable for studying waves with anisotropic wavenumbers.

1. Introduction

The fact that ocean internal waves transport large amounts of energy and momentum from generation to dissipation sites has been recognized and examined over the last few years (Niwa and Hibiya 2001; Ray and Cartwright 2001; Alford 2003; Buijsman et al. 2016; Ansong et al. 2017). In addition, dissipation of these waves is a key contributor to oceanic diapycnal mixing (Wunsch and Ferrari 2004; Kunze 2017). Therefore, knowing both internal wave generation sites and propagation paths can inform us of important geographic locations of internal wave dissipation and associated mixing. However, this knowledge is elusive; beyond not knowing the geography of many processes, we also do not know all the details of wave kinematics and dynamics. Here we present evidence of oceanic internal tides (internal waves at tidal frequency) being strongly refracted (a kinematic effect) by the Gulf Stream, a western boundary current that features a strong baroclinic jet, and explain the effects with ray-based wave propagation methods. Specifically, modal ray trajectories in the x, y plane of internal wave modes are computed and examined. In fact, the waves appear to be trapped in (ducted by) the jet, traveling upstream (Fig. 1), with only a fraction of the incident energy penetrating the baroclinic Gulf Stream currents.

The model product suggesting internal tide refraction and trapping (Fig. 1) is taken from a hydrodynamic global ocean model with realistic atmospheric and tidal forcing. The figure shows internal tide energy flux for the region; interaction of the internal tide and the current is strongly implied. To study and explain the trapping behavior in the Gulf Stream, and internal tide interaction with other subtidal-frequency and steady-state features, this paper first introduces ray-based methods for investigating internal tide modal propagation in baroclinic currents and then studies the internal tide–eddy field interaction.

Many studies have confirmed that low-mode internal tides propagate long distances (e.g., Ray and Mitchum 1996;

Corresponding author: Timothy F. Duda, tduda@whoi.edu

DOI: 10.1175/JPO-D-18-0031.1

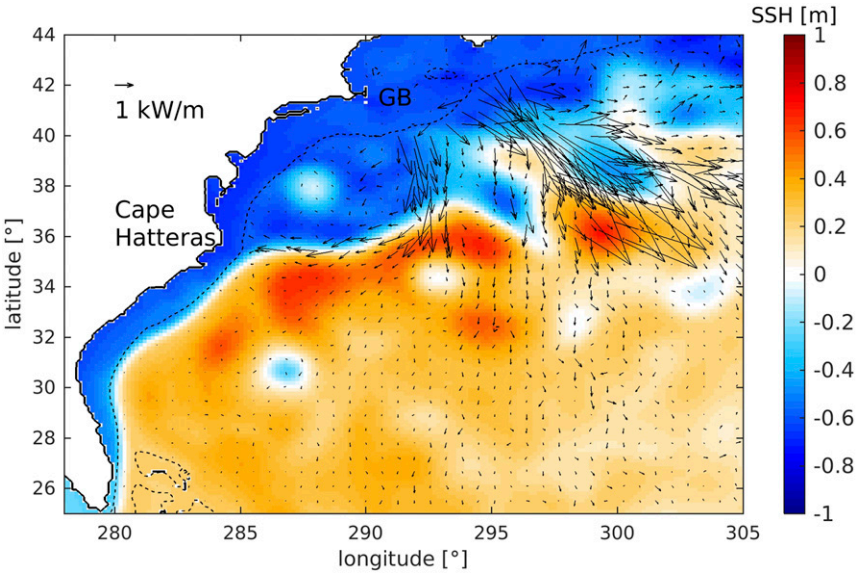

FIG. 1. Depth-integrated semidiurnal internal tide energy flux vectors and SSH (colors) extracted from the 8-km HYCOM simulation. Fluxes and SSH are averaged over the month of January 2012. Energy flux is the time-averaged vertically integrated product of the semidiurnal bandpass velocity vector and the pressure anomaly associated with semidiurnal vertical motions. The beam that radiates from Georges Bank (marked GB) appears to be trapped in the Gulf Stream, propagating upstream toward Cape Hatteras.

Dushaw et al. 2011; Li and Farmer 2011), but this does not mean that the waves are immune to loss mechanisms. Some internal tide energy may be transferred to subtidal flows or eddies through wave–current interactions, and another fraction may scatter into higher-mode waves more prone to immediate dissipation (Dunphy and Lamb 2014; Dunphy et al. 2017). Low-mode internal tides can be scattered into high modes by bathymetric roughness (Johnston and Merryfield 2003; Johnston et al. 2003; Mathur et al. 2014). Further conversion pathways are into high-frequency mode-one nonlinear internal waves (NIWs) in deep water (Li and Farmer 2011; Warn-Varnas et al. 2010), into mode-one NIWs on continental shelves immediately after generation (Sherwin 1988; Holloway et al. 1997), and into NIWs upon moving (as a long wave) from deep water to shallow water (implied by Nash et al. 2012). The resultant NIWs from these processes have high energy density and high shear and are prone to decay. Note that the propagated energy may also decay via the ubiquitous shear instability processes that continually erode the internal wave field (Kunze 2017). The point is that the generation and decay sites are far apart. Efforts to understand the distribution of internal tide source regions and sink (mixing) regions in the world's ocean, the details of propagation, and the effect on ocean circulation and climate represent an active research area supporting multiple approaches. The ray-based approach to wave propagation in baroclinic currents taken here is well suited to building understanding of energy propagation pathways and is complementary to coupled-mode approaches, discussed in the next paragraph. Ray-based (geometrical regime) analysis of waves is valuable for interpreting directionality of energy flux and is adopted here to interpret the energy flux patterns. Internal tidal modes propagating in barotropic currents have been previously examined using ray methods (Rainville and Pinkel 2006), but previously used ray methods are inadequate for examining the effects of baroclinic currents.

The interaction of the internal tide and the Gulf Stream has been studied in detail in two recent papers (Kelly and Lermusiaux 2016; Kelly et al. 2016). These papers use a coupled-mode propagation formalism to demonstrate that a southward-moving internal tide can be refracted by the Gulf Stream, which features strong baroclinic currents and horizontal density gradients. The ray-based analysis of this paper gives complementary insight into the paths of energy propagation. Importantly, Kelly and Lermusiaux (2016) show that the Gulf Stream produces regions of high mode-one internal tide energy-flux divergence, explained by tide-mean-flow terms in the mode-one energy balance. They also state that advection explains most of the tide-mean-flow interaction, suggesting that geometric wave theory explains mode-one internal tide interaction with the Gulf Stream, and demonstrate that internal tides can refract

strongly at an idealized jet representing the Gulf Stream, or reflect, depending on incident angle. The coupled-mode studies of the Kelly et al. (2016) paper offer an explanation for variable internal tide energy incident to the Middle Atlantic Bight area (Nash et al. 2012).

The main themes of this paper are to present some aspects of internal tide propagation in the Gulf Stream, then use the aforementioned ray-based (geometrical regime) approach to explain them. First, we present evidence from the global Hybrid Coordinate Ocean Model (HYCOM; Bleck 2002; Arbic et al. 2010) that the Gulf Stream (and other baroclinic jets, by analogy) can strongly refract and/or trap internal tide energy. We then explain this using a new combination of mode and ray analysis methods. The new methods should be generally applicable to transbasin baroclinic wave propagation studies. The ray method is chosen because it is suited to study refraction and wave ducting with more focus than the coupled-mode approach (Kelly et al. 2016). Removing coupling in the coupled-normal mode approach would be an alternative method for studying single-mode wave refraction that would add full wave phenomena such as diffraction but requires a more elaborate computation and diagnostic analyses to fully disclose refraction relative to a ray approach. Another alternative would be full computational approach such as used by Zaron and Egbert (2014), based on, for example, output from the model used to make Fig. 1. The computational approach can more fully and reliably quantify the effects of subtidal flow features on internal tide characteristics, but is not naturally suited to explaining the physics of the trapping.

The mode analysis here uses a new equation for properties of modes in arbitrary sheared background currents. The equation is a generalization of an existing equation by Jones (1967), while Jones' equation is itself a generalization of an equation used earlier (Eady 1949). A solution method for the equation is outlined. An important character of modes in shear is that the wave speed and modal shapes at a given location can be functions of wave direction, for example, the modal properties are anisotropic. It is convenient but incomplete to refer to the modes as having anisotropic wavenumbers, as there is also spatial dependence, that is, modal properties are heterogeneous. The local-mode approximation is adopted here, as there is no reasonable alternative.

The paper is structured as follows. Section 2 presents some of the current knowledge of internal tide generation and propagation. Section 3 shows HYCOM evidence for internal tide trapping (ducting) in the Gulf Stream. Section 4 presents equations for internal wave modes properties, including the general equation that allows sheared background currents and rotation. Section 5 presents ray equations for waves that have anisotropic wavenumbers (anisotropic phase velocity). Section 6 applies the ray-tracing method to modes propagating in a Gulf Stream area where they appear to be trapped, with mode properties being computed with the methods of section 4. Section 7 is a discussion and summary.

2. Internal tide generation and propagation

Internal gravity waves at the low end of the allowable frequency range for freely propagating waves are commonly found in stratified waters of the oceans. The waves at the lowest cutoff frequency are known as near-inertial waves, and those at or near the frequencies of tidal constituents are known as internal tides and as baroclinic tides. These waves are heavily influenced by the rotation of the earth. The basic properties of these waves and many details for specific oceanic scenarios are known (Vlasenko et al. 2005).

The world's barotropic tides drive baroclinic tides by the action of moving stratified water across gravitational potential surfaces at sloping bathymetric features. In general, this effect tends to form internal tidal beams that are vertically narrow, composed of many modes (Vlasenko et al. 2005; Garrett and Kunze 2007; Zhang and Duda 2013), but observations show that modal dispersion and dissipation lead to mode-one waves being strong and identifiable away from the source regions, both in deep ocean basins and on continental shelves (e.g., Sherwin 1988; Ray and Mitchum 1996; Alford and Zhao 2007; Dushaw et al. 2011; Klymak et al. 2011; Li and Farmer 2011; Zhao et al. 2016). At a given location and time, mode-one waves have vertical displacements throughout the water column that are all of the same sign, and behave much like interfacial internal waves in a two-layer environment, the simplest archetype environment that can support baroclinic waves. Mode-one ray trajectories are the primary subject of this paper.

Satellite observations of tidal-frequency surface elevations yield signals at the wavelengths of baroclinic internal wave modes, which are short with respect to barotropic waves, showing that baroclinic waves sustain substantial momentum and energy fluxes in many ocean regions. Mode-one waves dominate these observations, with fewer records showing identifiable propagating higher modes in the deep ocean (Johnston et al. 2003; Ray and Zaron 2016) and a few studies examining the conversion of mode-one waves to higher mode waves (Legg 2014; Haji 2015). Measurements from within the sea also show the dominance of mode-one waves, further supporting the hypothesis that mode-one internal tides carry a

substantial fraction of internal wave energy transport in the ocean. Kelly et al. (2013) argue that 50% of upper ocean semidiurnal internal tidal energy is contained in mode one, equaling 500 J m^{-2}, and that the flux rate into these tides globally is 0.21–0.3 TW, yielding a decay time scale of 7–21 days. Considering a typical group speed of 2.5 m s^{-1}, Kelly et al. (2013) show that these waves typically propagate 1500–4500 km before dissipation or conversion. For these reasons this paper concentrates on the propagation of mode-one internal tides, in isolation from many important generation, dissipation, and mode-conversion processes.

The results presented here build on some recent internal tide process studies. The fundamental physical effect of baroclinic tide generation by action of the barotropic tide at a sloping seabed is fairly well understood, but nuances of the process are still being examined and uncovered (e.g., Zhang et al. 2008; Zhang and Swinney 2014; Zhang and Duda 2013; Zhang et al. 2014; Paoletti et al. 2014; Zhang et al. 2017). Time dependence of the ocean imparts a subtidally time-varying transfer function to the process. Time-varying factors influential to baroclinic tide response are stratification (Gerkema et al. 2004), subtidal currents (Kerry et al. 2014; Lamb and Dunphy 2016), and incident internal tides (Kelly and Nash 2010).

Many works have addressed internal tide propagation from regional to large oceanic scales. Park and Watts (2006) used a ray trace method to model how currents act to deflect internal tide propagation paths, comparing results with field data. Ponte and Klein (2015) demonstrated the low-mode wave–eddy interaction by analyzing sea level in simulations. Dunphy et al. (2017) studied the pronounced effects of turbulent ocean eddies on low-mode internal tide propagation with a computational model, analyzing wave–"slow flow" interaction terms. Demonstrations of an ability to measure and study real-ocean internal tide signals were made by Dushaw (2002, 2003, 2006). This was followed by altimetric mapping of mode-one internal tides in the Pacific Ocean (Zhao and Alford 2009; Zhao et al. 2011), a data-based study of the Hawaii area (Zhao et al. 2010), and a study using both data and computational modeling to analyze generation and propagation south of Hawaii (Rainville et al. 2010).

3. Refracted and trapped internal tides

Interaction of coastally generated internal tides with the variable Gulf Stream has been analyzed by Kelly and Lermusiaux (2016) and suspected to cause intermittency of the internal tide conditions of the western North Atlantic. Motivated by this, internal tides were analyzed in ocean model output for this area. We use recent simulations of global HYCOM with a horizontal resolution of 8 km (1/12.5°) and 4 km (1/25°), which are discussed by Ansong et al. (2015) and Savage et al. (2017), respectively. The simulations employ atmospheric forcing from the Navy Global Environmental Model (NAVGEM; Hogan et al. 2014), geopotential tidal forcing for the five largest semidiurnal and diurnal tidal constituents, and linear wave drag to account for the unresolved high-vertical mode internal tide generation and to dampen low modes (Ansong et al. 2015; Buijsman et al. 2016). Following Buijsman et al. (2015), this wave drag is tuned to minimize tidal sea surface elevation errors with respect to the TPXO8 atlas (Egbert et al. 1994). Both the 8- and 4-km simulations feature 41 layers in the vertical direction. The HYCOM simulations with tides have been extensively compared with observations, and it has been found that the propagation of surface and low-mode internal tides have been accurately simulated (Shriver et al. 2012; Ansong et al. 2015; Buijsman et al. 2016; Ansong et al. 2017).

In this paper, we use hourly model data for the month of January 2012 for 8-km HYCOM and for 2 weeks in July 2014 for 4-km HYCOM. Only northwest Atlantic fields are processed. For both simulations, we compute the depth-integrated semidiurnal baroclinic energy fluxes $\mathbf{F} = (1/H)\iint \mathbf{u}' p' \, dz \, dt$ at hourly time steps, where $\mathbf{u}'$ and p' are the 10–14-h band-passed semidiurnal horizontal baroclinic velocity vector and baroclinic pressure anomaly, respectively; z is the vertical coordinate; t is time; and H is water depth (Buijsman et al. 2016). We compute monthly-mean semidiurnal energy fluxes and mean sea surface height (SSH) for the 8-km simulation, while we compute nonoverlapping 25-h mean energy fluxes and 48-h mean subtidal fields over a 14-day period for the 4-km simulation. The 25-h period is the average over two semidiurnal tidal cycles. The 48-h period is chosen to average over both semidiurnal and diurnal frequencies. The discrepancy in duration between the tidal flux and subtidal field averaging periods does not affect the analysis in this paper. Both the 8-km simulation in Fig. 1 and the 4-km simulation in all other figures in this paper show internal tide refraction, reflection, and trapping by the Gulf Stream. We perform a more in-depth analysis of the 4-km simulation because it has a more developed (sub)mesoscale field and its internal tide field is more time variable than in the 8-km simulation.

In Fig. 1, the trapping of the semidiurnal internal tide by the Gulf Stream in the 8-km simulation in an average sense is clearly seen, quantified by prominent high-valued mean energy flux vectors directed against the current jet. Internal tidal energy moving south from

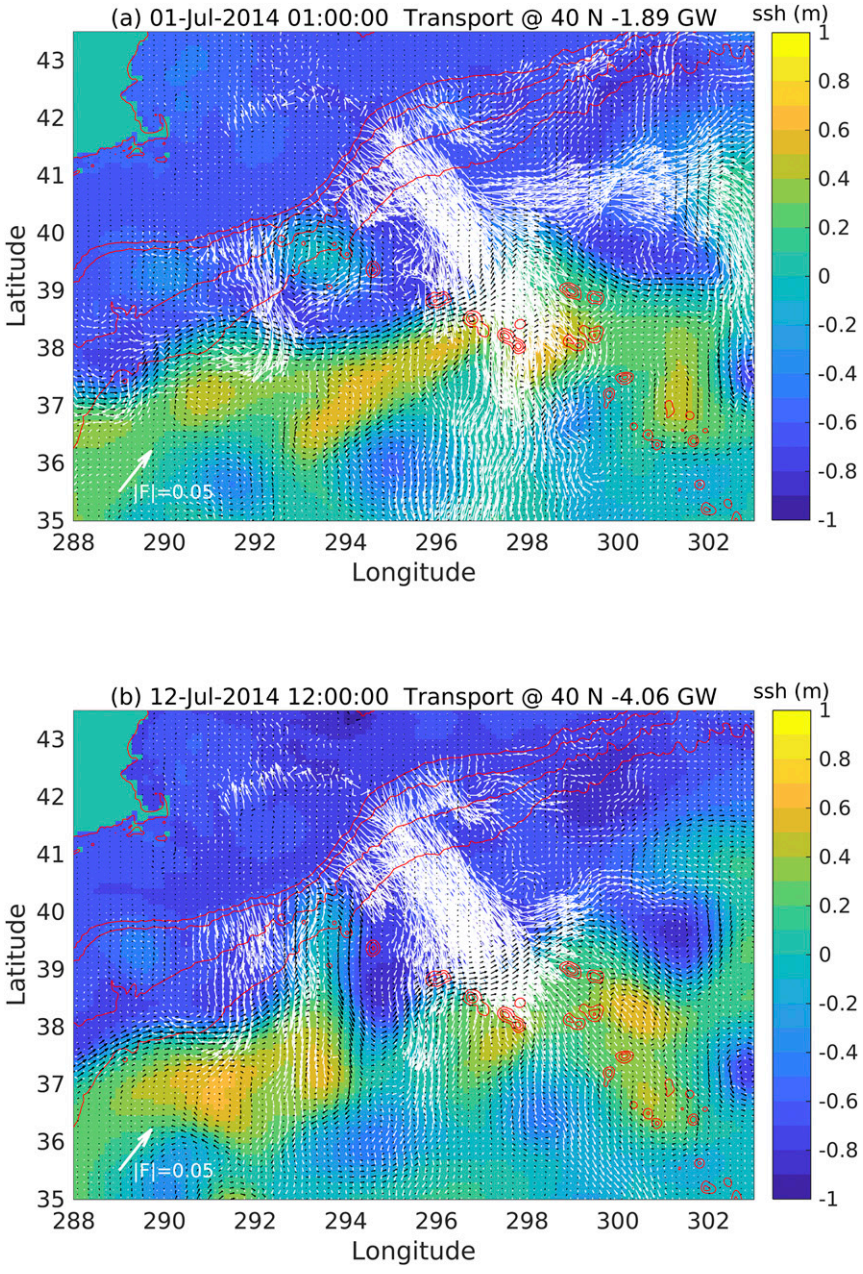

FIG. 2. Depth-integrated semidiurnal internal tide energy flux vectors, SSH (colors), and mean surface current vectors from the 4-km HYCOM simulation are shown for two time windows, each two semidiurnal periods in length. (a) A weak flux window, 1 Jul 2014. (b) A strong flux window, 12 days later. The arrow length for flux of 0.05 W m^{-1} is shown. Isobaths are shown for 0, 1000, 2000, 3000, and 4000 m.

Georges Bank that stems from the strong Gulf of Maine tidal currents appears to branch at 36°–37°N, with a flux of about 1 kW m^{-1} directed westward against the Gulf Stream main jet. Because the Gulf Stream meanders with a time constant much shorter than a month, the mean vectors are the sum of time-variable flux vectors. Flux vectors computed with a shorter time average of 25 h are shown in Fig. 2 for the 4-km simulation. It is apparent that the southward energy flux is interrupted by the Gulf Stream jet, quantified in Fig. 3. Upstream flux is visible in Fig. 2a. Using modal analysis and ray propagation methods, presented in the next two sections, we examine internal tide refraction and ducting in the Gulf Stream, and internal tide–current interaction more generally.

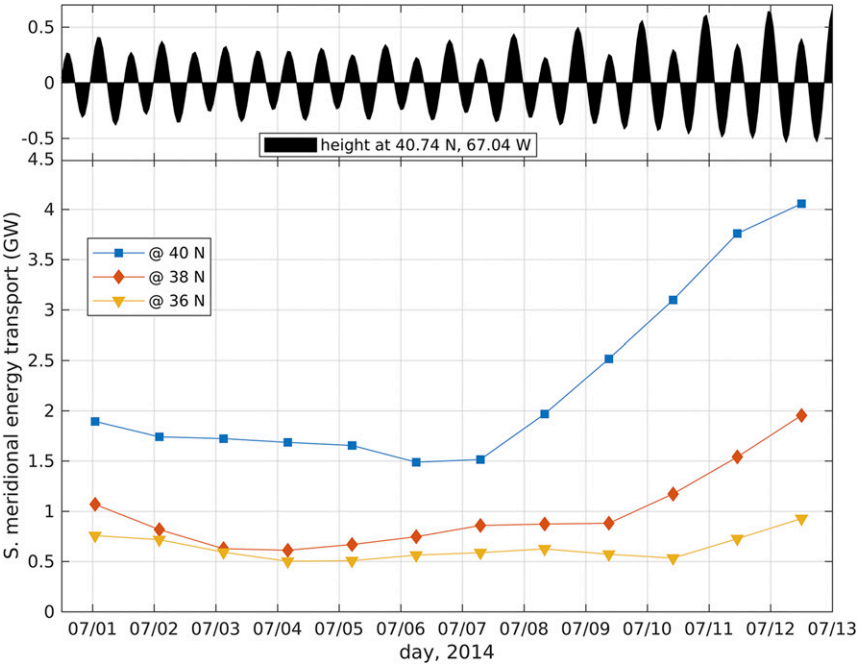

FIG. 3. Net meridional transport of internal tidal energy is plotted for 12 time windows extracted from 4-km HYCOM. At the top is the tidal height prediction (m) from the Oregon State University "East Coast" regional tide inverse model (http://volkov.oce.orst.edu/tides/otis.html) for a site on Georges Bank. The longitude range is 288°–303° (72°–57°W). See Fig. 2 to view the flux vectors for the first and last time intervals.

4. Internal wave mode properties in baroclinic currents

Typically the modal methods applied to internal tides use the normal modes of the system that stem from a separation of variables approach. These modes form a complete mathematical set but do not conveniently apply to situations with baroclinic currents, so we take an approach of using modes that explicitly include the effect of currents on the modal properties. In turn, the effect on modal properties drives an effect on propagation. The approach to finding the modes seeks solutions that are plane waves in the horizontal, so lateral uniformity is assumed at this point, often called the "local mode approximation" because it will yield different modes at different localities within a heterogeneous environment. With this approach, an equation governing internal gravity wave modal properties in a rotating fluid with uniform geostrophic currents that are everywhere parallel was derived some years ago (Jones 1967). A version of this equation extended to cover conditions of geostrophic currents that rotate with depth, and are thus two-dimensional, can be derived using identical methods. The Boussinesq approximation is used, and a small-amplitude (linear) approximation is made. For horizontally progressive harmonic waves of the form $\psi(x, y, z, t) = \hat{w}(z)\exp(-i\omega t + ikx + ily) = \hat{w}(z)\tilde{w}(x, y)\exp(-i\omega t)$, the extended Jones equation for modal properties is

$$\omega'(\omega'^2 - f^2)\frac{d^2\hat{w}}{dz^2} + 2\left[-f^2\left(k\frac{du_0}{dz} + l\frac{dv_0}{dz}\right) - i\omega' f\left(l\frac{du_0}{dz} - k\frac{dv_0}{dz}\right)\right]\frac{d\hat{w}}{dz} + \left[\omega'(N^2 - \omega'^2)(k^2 + l^2)\right.$$
$$\left. + \omega'^2\left(k\frac{d^2u_0}{dz^2} + l\frac{d^2v_0}{dz^2}\right) - i2f\left(k\frac{du_0}{dz} + l\frac{dv_0}{dz}\right)\left(l\frac{du_0}{dz} - k\frac{dv_0}{dz}\right) - i\omega' f\left(l\frac{d^2u_0}{dz^2} - k\frac{d^2v_0}{dz^2}\right)\right]\hat{w} = 0, \quad (1)$$

where f is the Coriolis parameter, $N(z)$ is the buoyancy frequency, and ω' is the depth-dependent intrinsic wave frequency in a Lagrangian frame following the geostrophic background current, that is, $\omega'(z) = \omega - ku_0(z) - lv_0(z)$. This equation reduces to the equation of Jones (1967) for parallel background flow. Jones' formulation specifies

TABLE 1. Comparison of different internal wave mode governing equations.

	Long wave	Standard internal wave	Long-wave Taylor–Goldstein	Taylor–Goldstein	Jones	New full equation
Finite wavelength		Included		Included	Included	Included
Rotation	c_p can be approximated	Included	c_p can be approximated		Included	Included
Barotropic flow		Allowed, with Doppler shift	Included	Included	Included	Included
1D baroclinic flow			Included	Included	Included	Included
2D baroclinic flow						Included

currents $u_0(z)$ only in the direction of k, but allows the wave to be in another direction (i.e., l can be nonzero). We call solutions of (1) the "full modes."

If the background current $\mathbf{u}_0(z) = (u_0, v_0)$ is set to zero, then $\omega'(z) = \omega$ and the governing equation reduces to the "standard" internal wave mode equation with rotation

$$\frac{d^2\hat{w}}{dz^2} + \frac{(N^2 - \omega^2)}{(\omega^2 - f^2)}|\mathbf{k}|^2\hat{w} = 0, \tag{2}$$

where wavenumber $\mathbf{k} = (k, l)$. If the background current is depth independent, the equation becomes

$$\frac{d^2\hat{w}}{dz^2} + \frac{[N^2 - (\omega - \mathbf{k}\cdot\mathbf{u}_0)^2]}{[(\omega - \mathbf{k}\cdot\mathbf{u}_0)^2 - f^2]}|\mathbf{k}|^2\hat{w} = 0, \tag{3}$$

which shows that the dispersion relation $\omega(k)$ consistent with (2) applies to waves in the Lagrangian frame. In the case of $f = 0$, the full equation reduces to the Taylor–Goldstein equation

$$\frac{d^2\hat{w}}{dz^2} + \left[\frac{N^2}{(U-c)^2} - |\mathbf{k}|^2 - \frac{d^2U/dz^2}{U-c}\right]\hat{w} = 0, \tag{4}$$

where $U = (\mathbf{k}\cdot\mathbf{u}_0)/|\mathbf{k}|$ is the background flow component parallel to the internal wave direction and $c = \omega/|\mathbf{k}|$. Only the background flow component parallel to the modal wave vector is relevant in the Taylor–Goldstein equation. Table 1 shows which of five physical effects are taken into account in each of six baroclinic mode equations.

The full-mode equation [(1)] is a fifth-order equation in wavenumber and is a polynomial eigenvalue problem. It can be solved for modal phase speeds (eigenvalues) $c_n(\theta)$ after conversion to a fifth-order polynomial function of the modal phase speed $c(\theta) = \omega/|\mathbf{k}|$ measured in the geographic coordinate system, where θ is the angle of the wave vector $\mathbf{k}$. In general, each $c_n(\theta)$ is anisotropic, and n indicates mode index. (Figures that show c_n for a single mode substitute c_p for c_n.) It is also important to note that because c is the phase velocity in the Eulerian reference frame tied to Earth's surface, the effects of baroclinic and barotropic horizontal flow on the wave propagation are subsumed into the modal properties. Using the standard solution methods for polynomial eigenvalue problems (Tisseur 2000), a solution is formed that is a function of the desired modal profile $\hat{\omega}(z)$. The solution functions (built from the mode shapes) are orthogonal, but the mode shapes $\hat{\omega}(z)$ are not. Figure 4 shows properties of modes one and two computed using example current and stratification profiles for a location in the Gulf Stream, with fields extracted from 48-h averaged (detided) 4-km HYCOM model output. Mode one has a minimum

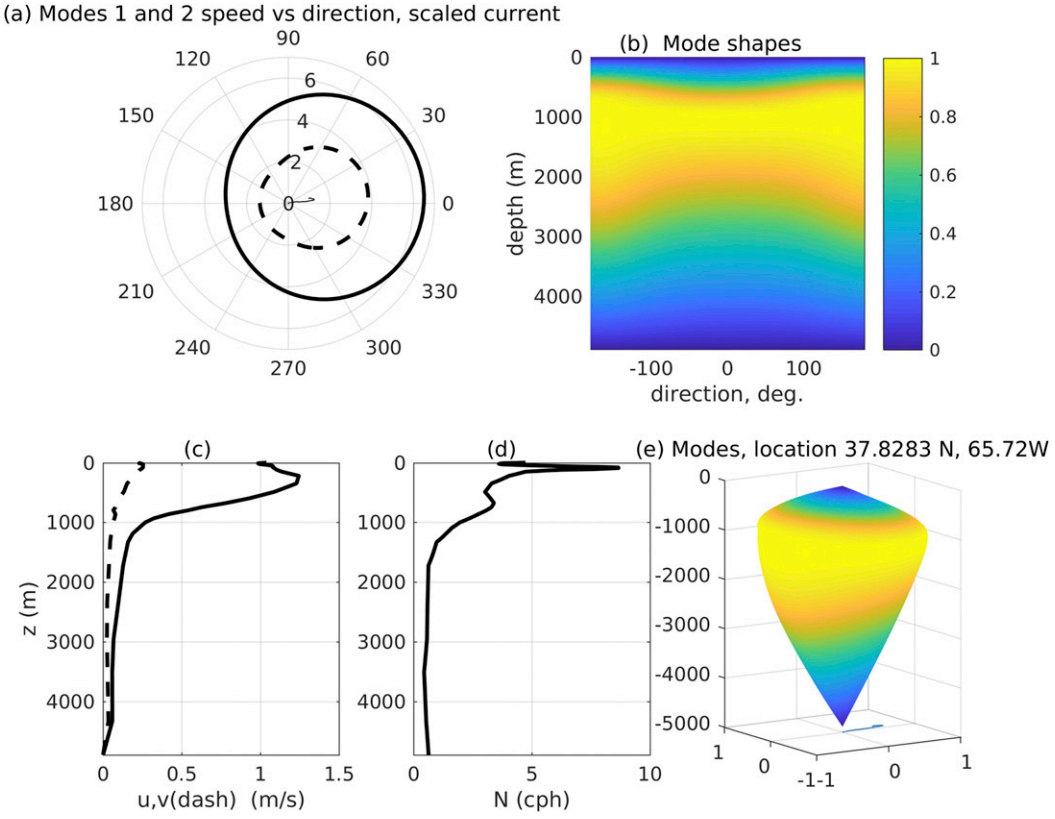

FIG. 4. Mode properties are computed for conditions extracted from the 4-km HYCOM simulation. (a) Phase speed ($\mathrm{m\,s^{-1}}$) for modes one and two as a function of wave direction (zero is eastward, anticlockwise sense). The phase speeds $c_1(\theta)$ and $c_2(\theta)$ for modes one and two resemble circles but are not. The black line is the current hodograph. (b) The magnitudes of the mode-one shapes are shown as a function of wave direction. (c) The east u and north v current profiles. (d) The N profile. (e) A surface depiction of mode-one magnitude mapped onto wave direction. The x and y axes of the plot are east and north, respectively, with a scaled version of the eastward (x directed) current hodograph shown at the 5000 m depth. The modes directed eastward appear nearly triangular with respect to depth, and the westward modes are more curved.

speed in the direction ~270°, opposite the Gulf Stream baroclinic jet, enabling trapping of energy because rays in directions slightly above or below the direction of minimum could be refracted back into and across the jet center axis, cyclically. Figure 5 shows modal properties computed using the conditions used in Fig. 4, with the single alteration of using barotropic currents in place of the current profiles to obtain the solutions. Modal properties computed with these differing current fields are quite different. Note that the strength of the current at the location of highest density gradient has a major effect on mode-one anisotropy, so that using the smaller barotropic current in place of the baroclinic current reduces the mode-one anisotropy.

5. Ray tracing of modal waves with anisotropic speed

Baroclinic mode propagation can be described in general terms by a system of coupled mode equations (Pierce 1965; Kelly et al. 2016). In many situations the mode coupling is weak because very pronounced bathymetry is required for strong coupling (Johnston and Merrifield 2003; Johnston et al. 2003; Kelly et al. 2016) and the equations can be decoupled under the adiabatic approximation (Milder 1969). In this approximation the modes do not exchange energy and the propagation of each mode can be described by the Helmholtz equation (Rainville and Pinkel 2006; Zhao et al. 2016). The coupled-mode approach requires that modes be orthogonal, which the full modes are not, so that approach can only be approximate if full modes in baroclinic flows are used. However, if the coupling terms that link the equations are weak (adiabatic approximation), the behavior of a mode can be studied in isolation from the others with reasonable accuracy.

The behavior of waves with anisotropic speed is discussed in general terms by Landau and Lifshitz (1960). A key aspect of the waves, proven elegantly in the book,

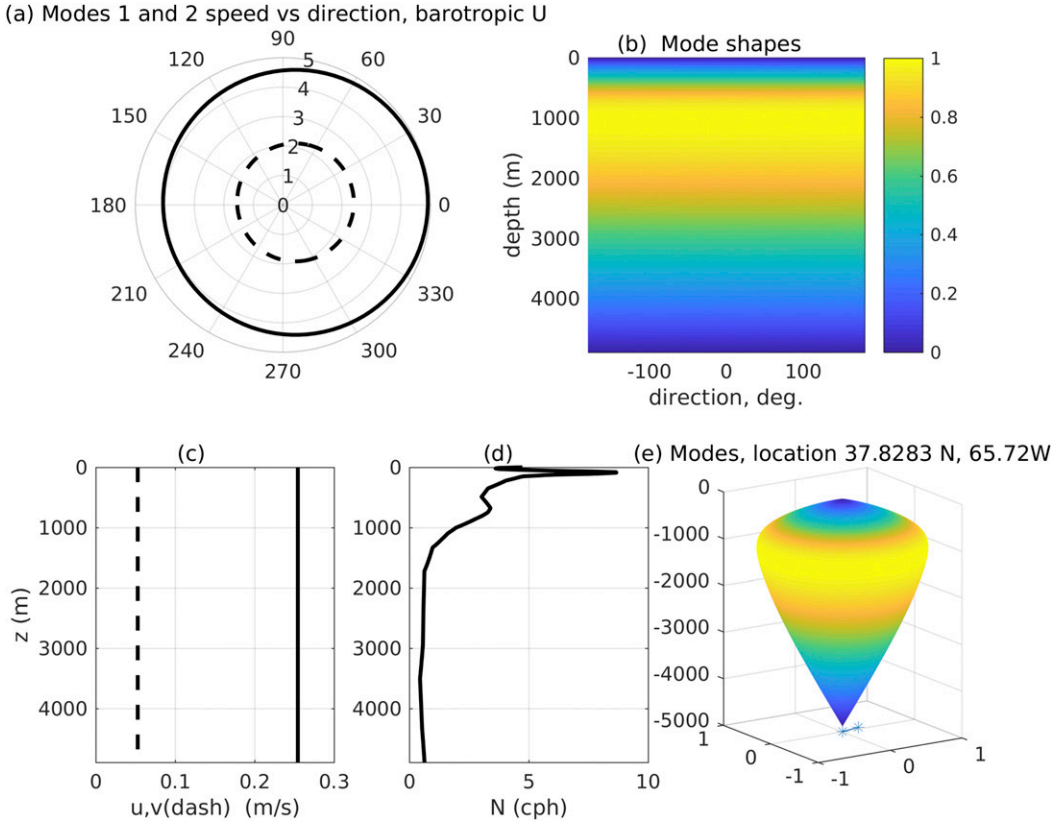

FIG. 5. Conditions and modes are shown as in Fig. 4, but the barotropic current is substituted for the depth-dependent current. (a) Phase speed ($\mathrm{m\,s^{-1}}$) for modes one and two as a function of wave direction (zero is eastward, anticlockwise sense). (b) The magnitudes of the mode-one shapes are shown as a function of wave direction. (c) The east u and north v current profiles. (d) The N profile. (e) A surface depiction of mode-one magnitude mapped onto wave direction. The current vector is shown at 5000 m depth.

is that the ray direction (the direction of energy propagation) for waves with a defined phase front is normal to the local wave-vector surface (k surface). Because $c(x, y, \theta) = \omega/k(x, y, \theta)$, it follows that $k(x, y, \theta) = \omega\, S(x, y, \theta)$, and that the $k(x, y, \theta)$ surface coincides with the slowness $S(x, y, \theta)$ surface for fixed ω, where $S = 1/c$. In this situation, the well-known ray equations that apply to waves with isotropic S do not apply. Numerous works address the properties and kinematics of these waves in elastic media, including in the fields of nondestructive testing (e.g., Newberry and Thompson 1989) and seismology (e.g., Červený 1972; Vavryčuk 2006). Note that the requirement of horizontal uniformity (the local mode approximation) has been relaxed for wave propagation analysis.

For the common situation of a wave with isotropic S in a nonmoving two-dimensional medium, the S surface is a circle and the normal is always directed outward on a radial. Thus, rays are normal to the phase front. Another common situation is a wave propagating in a current. Here, the phase fronts are not always aligned with the energy-flow direction (the ray direction) because the wave may be advected and thus "crab" sideways relative to the normal to the phase fronts. This is treated in some detail by Uginčius (1972), who derives the Lagrangian function for the situation. The wave-in-current situation is one specific example of a wave with anisotropic slowness. In that situation, the function $S(x, y, \theta)$ is equal to the inverse of the sum of the scalar wave speed $c(x, y)$ and the projection of the current $\mathbf{u}(x, y)$ in the direction θ.

As mentioned, the energy-propagation paths of progressive horizontal modal waves of form $\exp(ikx + ily - i\omega t)$ can be studied in the geometrical regime using ray tracing. This regime is defined by the wavelength λ not changing too abruptly within the spatial domain, $d\lambda/dx \ll \approx 18$ (Elmore and Heald 1985). General equations for rays in three-dimensional inhomogeneous and anisotropic elastic media are given by Červený (1972), but these are intricate and are not in a convenient form for the study of baroclinic tides in the ocean waveguide. The mode equation

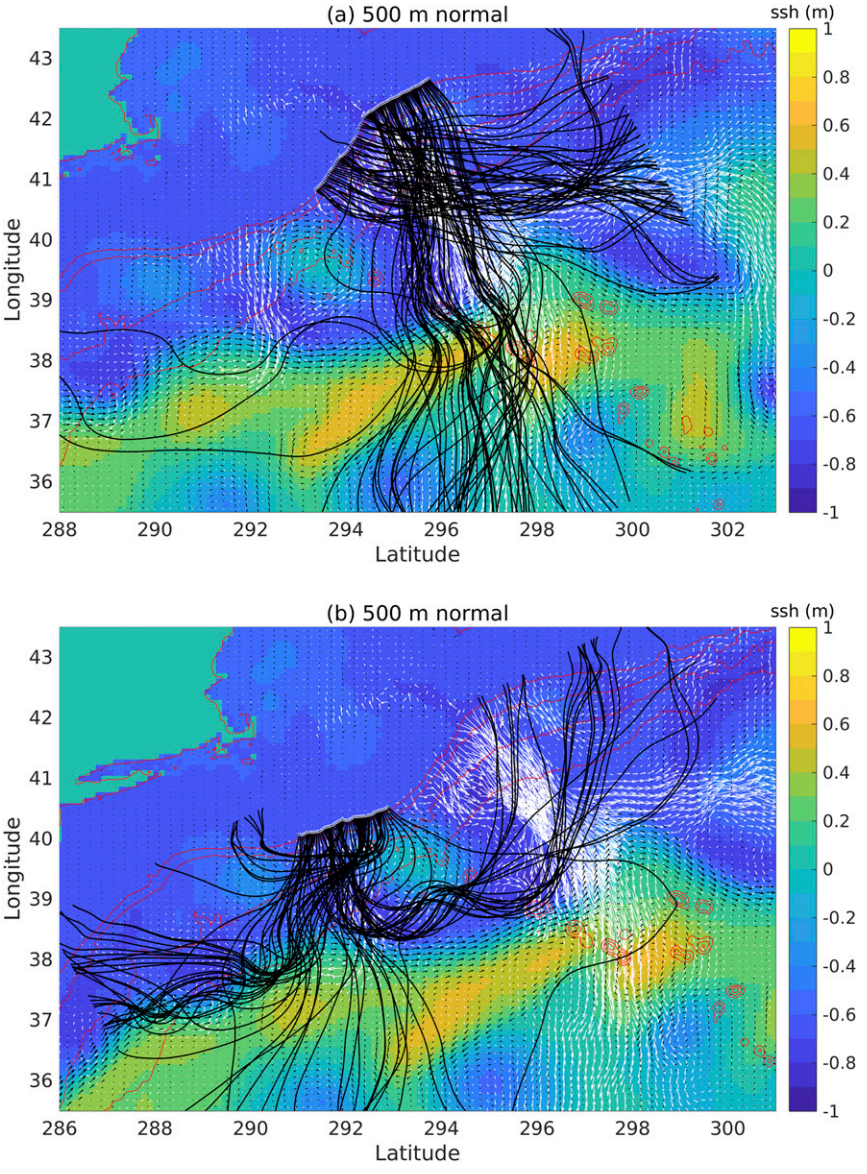

FIG. 6. M_2 internal tide rays, bathymetry, SSH, energy flux vectors (see Fig. 2), and 48-h surface currents are shown. The conditions are the time mean of the 1–2 Jul 2014 48-h window of 4-km HYCOM output (days 182–183). The rays are initialized at the 500-m isobath directed into deep water. Isobaths shown are 0, 1000, 2000, 3000, and 4000 m. The maximum current speed is 2.28 m s^{-1}. (a) Rays corresponding to the east flux beam. (b) Rays corresponding to the west flux beam.

of the previous section allows direct computation of $k(x, y, \theta)$ and $S(x, y, \theta)$ for a given frequency ω, so that only the proper ray equations for the case of anisotropic S on a plane are needed to complete the solution. In addition to the ray direction angle β that is part of every ray solution, a new angle α, the angle of the normal to the phase front of the propagating signal, comes into play. Using the angle notation of Uginčius, the general ray equations are (see the appendix for derivation)

$$\frac{dx}{ds} = Q\left[S(\alpha)\cos\alpha + \sin\alpha\frac{\partial S}{\partial\theta}\bigg|_{\theta=\alpha}\right],$$

$$\frac{dy}{ds} = Q\left[S(\alpha)\sin\alpha - \cos\alpha\frac{\partial S}{\partial\theta}\bigg|_{\theta=\alpha}\right],$$

$$\frac{dp_x}{ds} = QS(\alpha)\frac{\partial S}{\partial x}, \quad \text{and}$$

$$\frac{dp_y}{ds} = QS(\alpha)\frac{\partial S}{\partial y}, \tag{5}$$

with normalization factor

$$Q = \left[S^2(\alpha) + \left(\frac{\partial S}{\partial \theta}\bigg|_{\theta=\alpha} \right)^2 \right]^{-1/2}. \quad (6)$$

The angle $\alpha(x, y) = \arctan(p_y/p_x)$ is the direction of a vector normal to the phase front, with $p_x = \partial\phi/\partial x$ and $p_y = \partial\phi/\partial y$ being phase derivatives. The slowness value $S(\alpha)$ is the slowness evaluated at the phase-normal angle, $S(x, y, \alpha)$ with x and y dependence suppressed in the notation. The coordinates (x, y) define the ray trajectory which has length increment ds. An auxiliary quantity that emerges from integration is the slope of the ray path M, given by

$$M = \frac{dy}{dx} = \tan\beta = \frac{S(\alpha)\sin\alpha - \cos\alpha \dfrac{\partial S}{\partial \theta}\Big|_{\theta=\alpha}}{S(\alpha)\cos\alpha + \sin\alpha \dfrac{\partial S}{\partial \theta}\Big|_{\theta=\alpha}}. \quad (7)$$

At any position on the trajectory the ray angle is $\beta(x, y) = \arctan(M)$. Implementing the equations requires the field $S(x, y, \theta)$ in the region of the computed ray trajectory and the specification of the starting phase-front normal angle α. An initial β can be given and the consistent initial α can be found because the equation for M can be rearranged to yield $\tan\alpha$ as a function of β with initial guesses for α and its angular derivative, and iterated until convergence. For the case of isotropic S (i.e., $\partial S/\partial\theta = 0$) these equations reduce to established ray trajectory equations. In the isotropic case $\alpha = \beta$ (skew angle $\alpha - \beta = 0$.)

The ray equations given by (5) and (6) are more compact than a set of more general ray equations (Červený 1972), which is understandable because the equations given here are valid only for waves traveling in two dimensions acted on by fewer restoring forces than exist for waves in elastic media.

6. Ray trajectories in the Gulf of Maine/Gulf Stream region

The next step in examining modal wave propagation behavior in the Gulf Stream region is to compute ray trajectories using the mode and ray-tracing tools. The mode analysis provides the capability to produce anisotropic internal tide modal phase speed fields in this region having sheared subtidal flow, and the generalized ray equations allow the effect of the speed anisotropy to be included. The phase-speed field computation requires background current and stratification over the domain. These are taken from 48-h averages of the 4-km HYCOM fields, with the averaging process attenuating

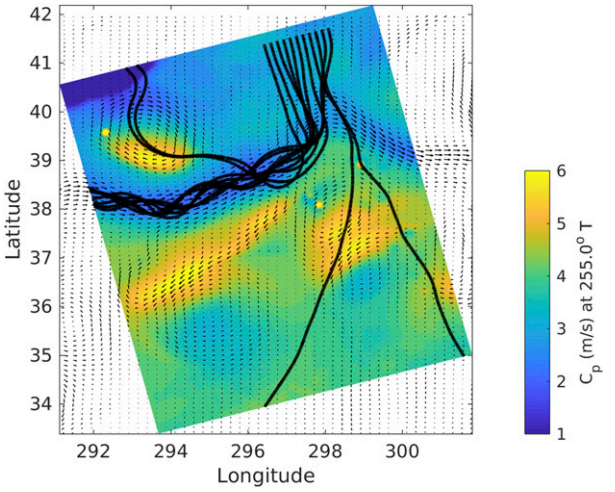

FIG. 7. Ray trajectories for M_2-frequency mode-one internal tides moving south from the Gulf of Maine area are shown. The colors show the modal phase speed for waves moving at heading 255° (parallel to the slanted top of the computational domain). The arrows show the surface current speed and direction. The maximum current is 2.08 m s^{-1}. The full-mode equation [(1)] and the anisotropic ray equations [(5)] are used.

the effects of internal tide. Figure 6 shows mode-one ray trajectories. The figure also shows bathymetry of the study area, the surface current vectors for the period 1–2 July 2014, the internal tidal energy flux, the SSH, and one set of rays computed for this time period. The rays are computed using the depicted fields, the full modes [(1)], and anisotropic ray tracing [(5)]. The rays represent trajectories for mode-one M_2 internal tides moving south from the 500-m isobath of the continental slope south-southeast of the Gulf of Maine and Georges Bank area of strong tides and strong internal tides. The ray paths loosely follow the energy flux vectors, showing a general agreement of the ray trajectories and the energy flux computed from the model fields. There is not one-to-one agreement, but only a single mode propagating adiabatically is considered, and it should not exactly replicate the HYCOM fluxes that include approximately the first five modes. Also, note that multiple interfering waves in HYCOM would yield flux point vectors that would not represent the actual fluxes (e.g., nodes can occur); spatial averaging would be required to disclose flux. Trajectories moving upstream in the Gulf Stream jet are seen in both panels of Fig. 6. The eastward trajectories at 40°N, 299°E in Fig. 6a clearly refract to the north away from the surface jet, while westward rays cross the jet. Most of the rays in Fig. 6b, from the western source region, occupy the jet. Fewer than half the rays transit the Gulf Stream because of the trapping and the

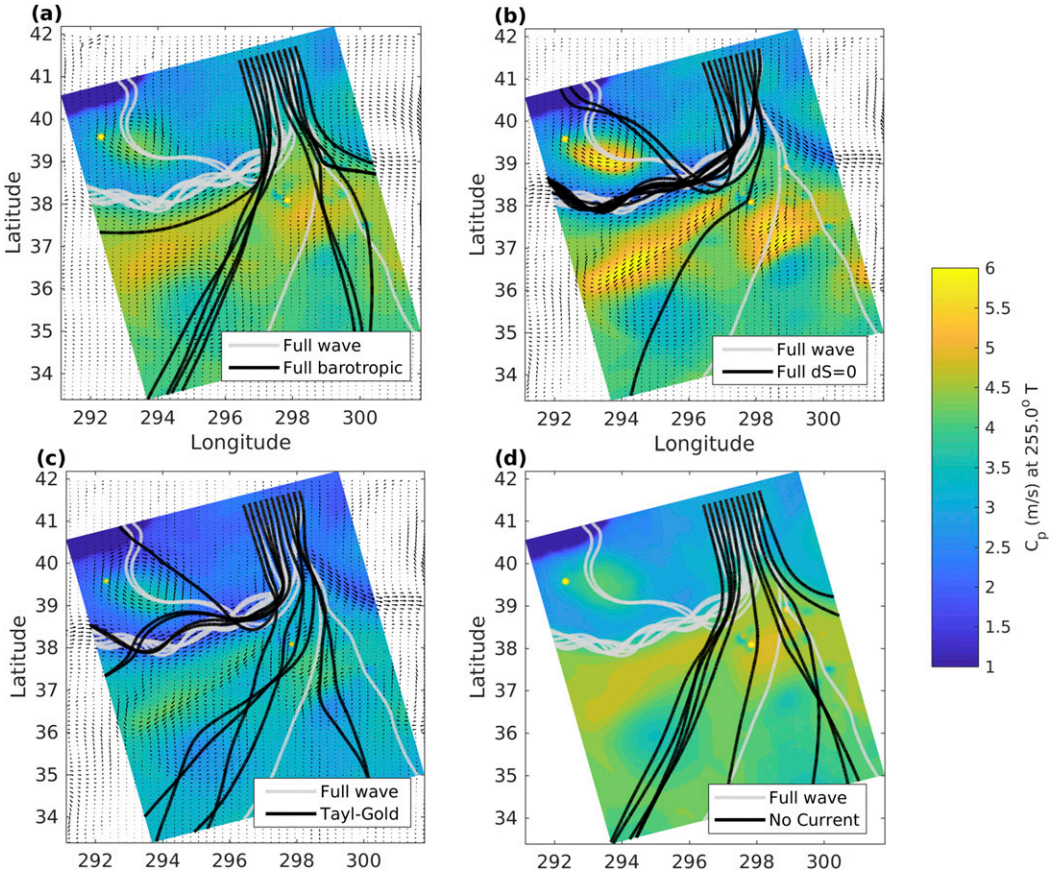

FIG. 8. (a) The black lines show the full-mode M_2 internal tides ray trajectories computed as in Fig. 7 with the exception that the barotropic currents at each location are used. The background colors show the modal speed at wave heading 255°. The maximum current is 0.57 m s^{-1}. The full-mode rays of Fig. 7 are shown in white in all panels. (b) The black lines show the full-mode M_2 internal tides ray trajectories computed as in Fig. 7 with the exception that $\partial S/\partial\theta$ is set to zero in the ray equations. (c) The black lines show M_2 internal tides ray trajectories computed using anisotropic phase speed fields resulting from the Taylor–Goldstein mode equation [(3)]. (d) The no-current rays that correspond to stratification-only sensitive modes [(2)] are shown with black lines. In (d) the colors show the isotropic phase speed (speed at 255° and all other directions).

avoidance, suggesting that less than half of the energy will cross the jet.

The steps to compute internal tide ray trajectories are to produce mode-one phase speeds at the required azimuths within the domain, then integrate the ray equations. In practice, the slowness is only needed in a span of angles surrounding parallel to the ray trajectory in order to obtain the ray-tangent slowness and the azimuthal gradient of slowness. Figure 7 shows a second example of ray tracing for full-mode semidiurnal M_2 mode-one internal tides moving south from the Gulf of Maine. The rays begin at azimuth 165° somewhat offshore of the continental slope. The ray starting locations are separated by ~14.5 km. Seven of the 11 rays turn and become trapped traveling upstream against the Gulf Stream jet. Two other rays turn into the jet in the same way and are nearly trapped, but strongly refract at the south boundary and escape to the north. Two rays are not trapped and continue southward. The rays in the jet refract repeatedly in the duct created by the phase speed minimum for rays directed upstream in the jet. The clockwise bend in the jet facilitates the trapping by reducing the angle between the jet and the rays on the south side of the jet.

a. Dependence of trapping on mode property and ray trajectory approximations

The trapping behavior of the full-mode rays is now analyzed by altering the mode and ray models. First, the effect of the background current being sheared is studied by examining ray behavior in the barotropic flow. This is done by calculating the mean current at each location and then solving the full-mode equation [(1)] with these barotropic currents substituted in place of the

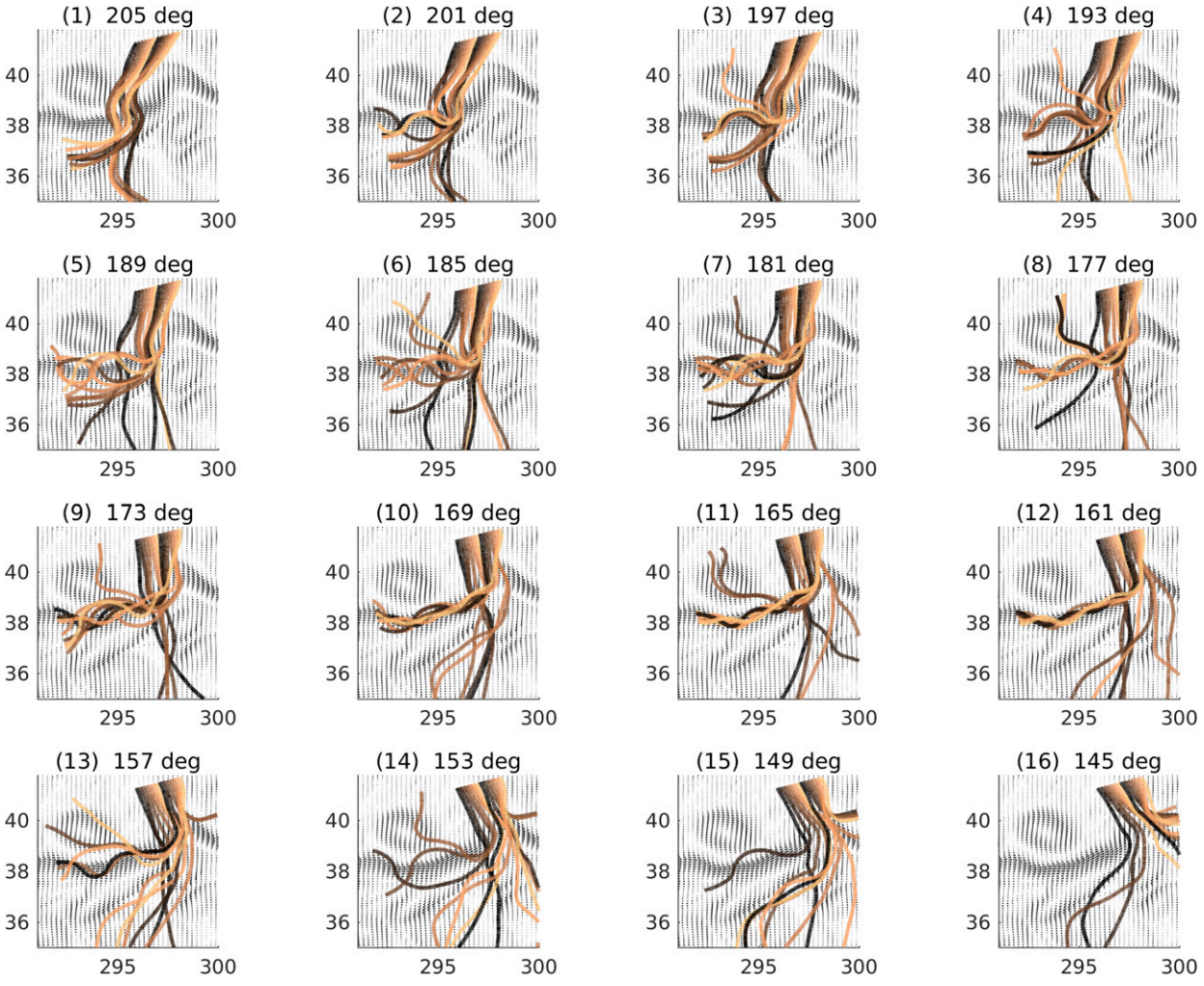

FIG. 9. Rays are plotted from one set of initial positions and many initial angles, as indicated. Small arrows on a grid show the surface current. Trapping occurs for angles of 149°–201°, with trapping proclivity varying strongly between the simulations.

current profiles. Figure 8a shows the resulting rays. The rays computed using the barotropic current approximation do not refract as much as the baroclinic current rays, and none are trapped. Next, the effect of the $\partial S/\partial\theta$ terms in the ray equations [(5)] is examined by setting it to zero (i.e., the isotropic ray equations are used). For this test, the anisotropic nature of S is otherwise retained. The full-mode solutions with baroclinic current are used. The results (Fig. 8b) show that the ray trajectories depend on whether this term is included. The figure shows that the existence of trapping is not dependent on the action of the $\partial S/\partial\theta$ term, but that trajectory details are. Interestingly, the northbound rays with and without this term included pass on opposite sides of a strong eddy.

To examine ray trajectory dependence on whether the complicated full-mode computation must be made, we compare the full-mode ray trajectories to those that result if the Taylor–Goldstein mode equation [(4)] is used, or the no-current internal wave equation [(2)] is used. Figures 8c and 8d show that invoking the approximations inherent in these equations yields entirely different trajectories and reduced trapping tendency.

b. *Geometrical aspects of rays and ray trapping*

All aspects of the ray initial conditions influence the likelihood of rays becoming trapped in the current jet. For example, tests demonstrate that small changes in ray starting positions and angles cause large changes in ray paths. To further analyze the ray capture (trapping) behavior in the duct, rays are started at many angles. Figure 9 shows the sensitivity of the trapping to ray initial angle. For 14 ray origins, rays are initially directed

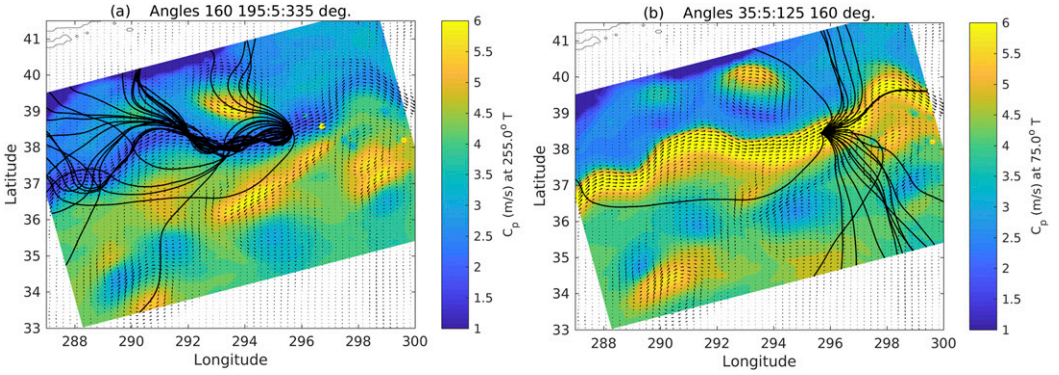

FIG. 10. Rays from a single point in the jet initiated at a series of angles are plotted. (a) Rays originating upstream; initial angles are indicated. (b) Rays originating downstream. The ray at angle 160° is shown in each plot. Surface currents are shown, and phase speed at one angle is shown with color in each frame. Rays at 195°–300° directed upstream in the jet are effectively trapped for a few hundred kilometers, a 105° angular spread for trapping, so that the critical angle for the duct at this time and location is approximately 50°.

at 16 differing angles. Rays are trapped over a wide range of initial angles.

Figure 10 shows full-mode rays traced from a point in the jet using the generalized ray equations [(5)]. Rays are initialized at a 5° interval. Rays directed downstream diverge and exit the jet, whereas rays over about a 100° span heading upstream become trapped. This means that rays encountering the jet with grazing angles of less than about 50° are prone to trapping, or equivalently that the critical angle for the jet duct is 50°.

c. *Temporal evolution of ray behavior*

Figures 11 and 12 show rays originating in the Gulf of Maine region computed for conditions in six consecutive nonoverlapping 2-day time windows. Figure 11 shows rays in the western flux beam region (Figs. 2, 6) starting at a

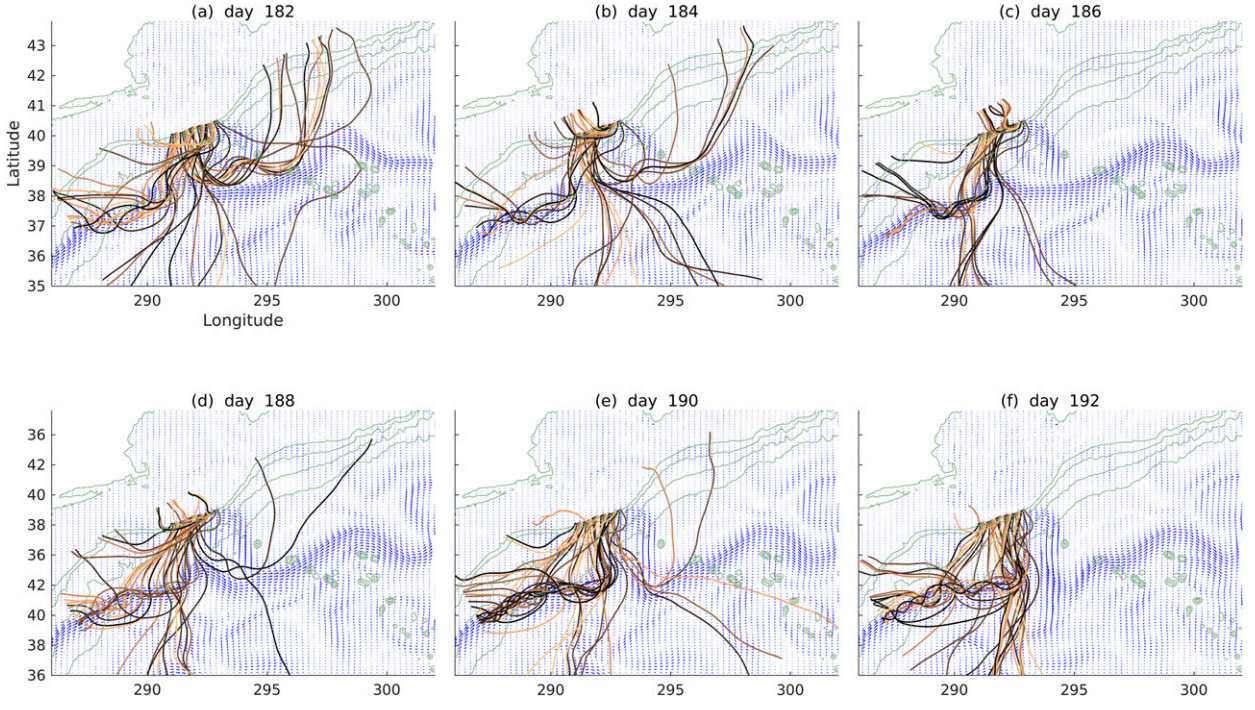

FIG. 11. Rays moving outward from the 500-m isobath in the western beam are plotted for six 2-day nonoverlapping time windows. Thirty-eight rays are shown starting at 68°58.5′W (291°1.5′E) with an increment of 3′ longitude. Surface currents are shown. Isobaths are shown at 1000-m interval up to 4000 m.

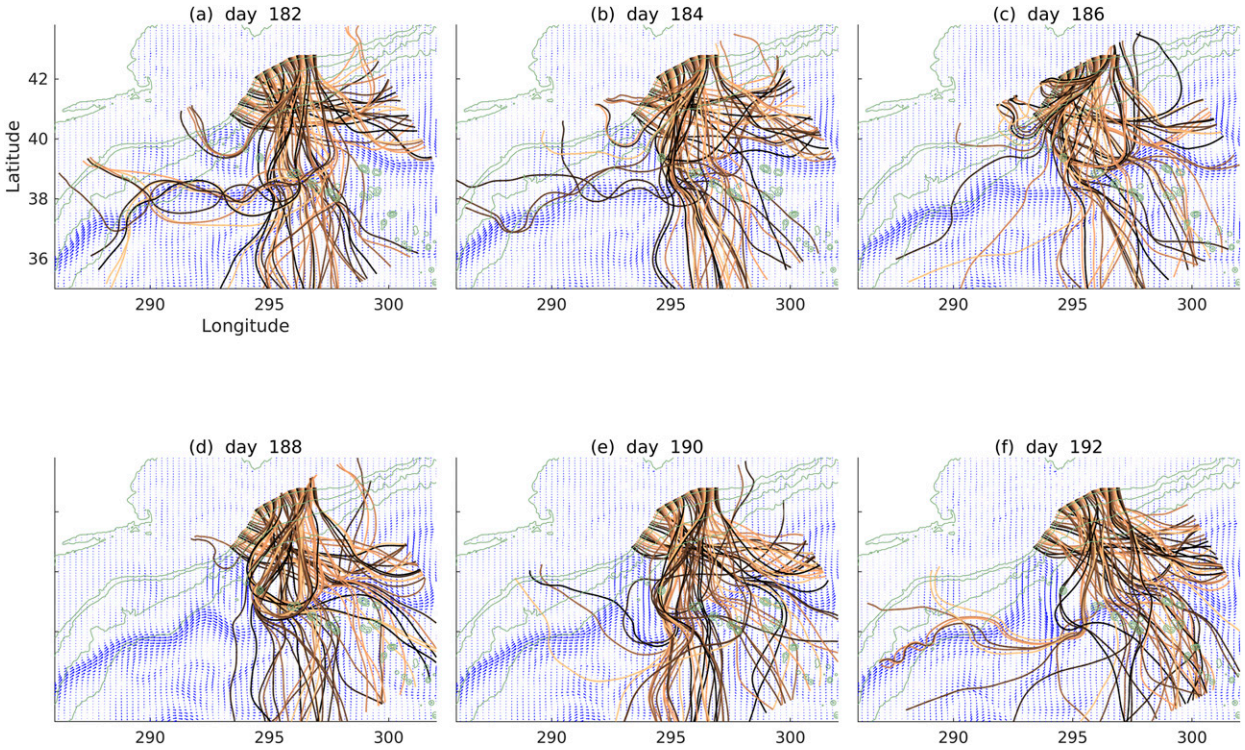

FIG. 12. Rays moving outward from the 500-m isobath in the eastern beam are plotted for six 2-day nonoverlapping time windows. Seventy-three rays are shown starting at 66°38.952′W (293°21′E) with an increment of 3′ longitude. Currents and isobaths are shown as in Fig. 11.

smoothed version of the 500-m isobath at an angle normal to the smoothed isobath. Figure 12 shows rays for the eastern beam region created with the same method. For the western beam, typically fewer than 10 of the 38 rays plotted penetrate through the Gulf Stream, so that approximately three quarters of the energy is strongly refracted and shows either the upstream-directed ray trapping behavior or downstream ray-diverence behavior. Rays that are directed obliquely toward the jet in the downstream orientation see the jet as an antiduct rather than a duct and are repelled at the northern edge of the jet. The time variability of the eastern beam is perhaps more pronounced than for the western beam. The number of eastern beam rays trapped in the duct ranges from zero to six, and the geometry of the ray group directed to the east is highly variable. The geometry of the rays that penetrate the Gulf Stream is variable for both beams.

Figure 13 shows six panels of 300 rays each, equally spaced in longitude, originating roughly normal to the 500-m isobath as in Fig. 11. Here, a small random deviation angle from isobath-normal is introduced to each ray to represent internal tide generation uncertainty. Three groups, of two panels each, show rays for each of three time periods (i.e., for three background ocean states). The ray patterns differ substantially with respect to time, but introducing the angular variability causes less variation. One notable feature is that larger areas with no rays are predicted to form and to subsequently fill in with rays, with a time scale of a few days.

d. *Validity of ray tracing*

Next, to check whether the background field has spatial variations that are consistent with ray tracing, the spatial derivatives of the internal tide mode-one wavelength λ are computed to see if the criterion $|d\lambda/dx| \ll 18$ is met. Figure 14 shows this using wavelengths computed for two mode propagation directions, westward (direction index 9 of 36, heading 255° in the computation) and southward (direction 18, 165° heading). The gradients are typically between -2 and 2, with only one location not influenced by bathymetry being below -3 (at $[x, y] \sim [200\,\text{km}, 0]$).

e. *Long-range ray tracing*

The ray trajectories computed for internal tides propagating into the Gulf Stream from the Gulf of Maine area show very strong refraction. There are, however, large areas of the ocean where the refraction from the mesoscale fields will be far less. Figure 15 shows rays for a larger section of the 4-km HYCOM western North Atlantic field outputs. The rays are in two groups with a gap so that rays

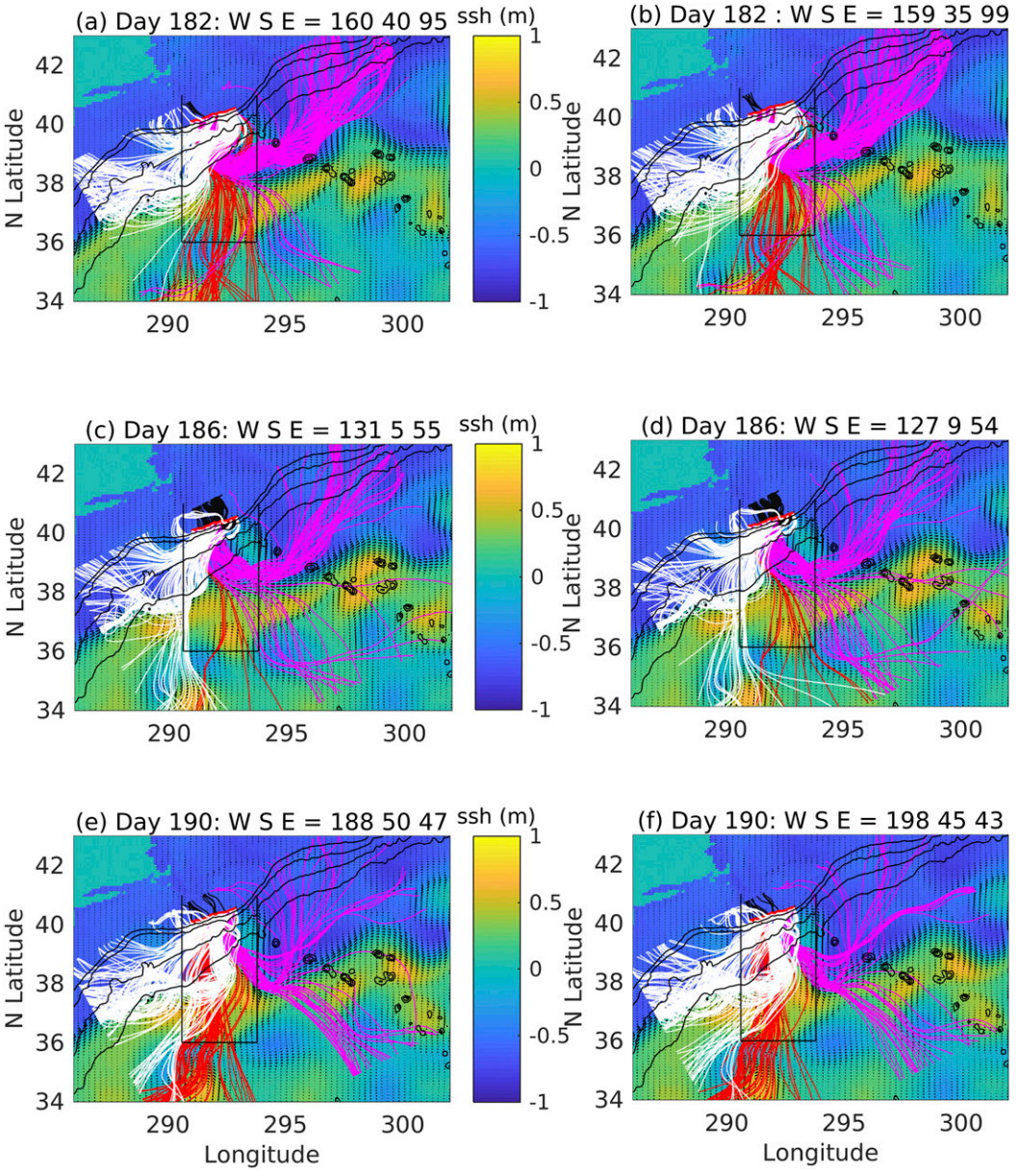

FIG. 13. Many rays originating in the western beam area are plotted for mean field conditions for three 48-h windows extracted from the 4-km HYCOM simulation. Rays start at the smoothed 500-m isobath in directions normal to the isobath, each with an addition random perturbation angle taken from a group with zero mean and standard deviation 2°. The perturbations allow ray-path sensitivities to initial conditions to be examined. Each panel shows 300 rays. Each panel also shows three lines, with rays crossing the western line shown in white, rays crossing the southern line in red, and rays crossing the eastern line in pink. The quantities of each color of ray are printed above each panel (W, S, E corresponding to white, red, pink). (a) Rays for day 182 window, angle perturbation set 1. (b) As in (a), but angle perturbation set 2 is used. (c) Rays for day 186 window, angle perturbation group 3. (d) As in (c), but perturbation set 4 is used. (e) Rays for day 190 window, angle perturbation group 5. (f) As in (e), but perturbation set 6 is used.

do not pass over the Corner Rise Seamounts where high modal wavenumber gradients will be present. The rays start at heading 275°. The northern group shows a caustic at (39.5°N, 312°E) near the ray origins, and some of the rays become trapped in the Gulf Stream jet (area of low c_1, indicated as c_p in the plot). The southern group shows much less refraction than the northern group because the model property gradients are weaker. The existence of relatively straight rays in areas with weaker eddy activity is in agreement with observations (Zhao and Alford 2009).

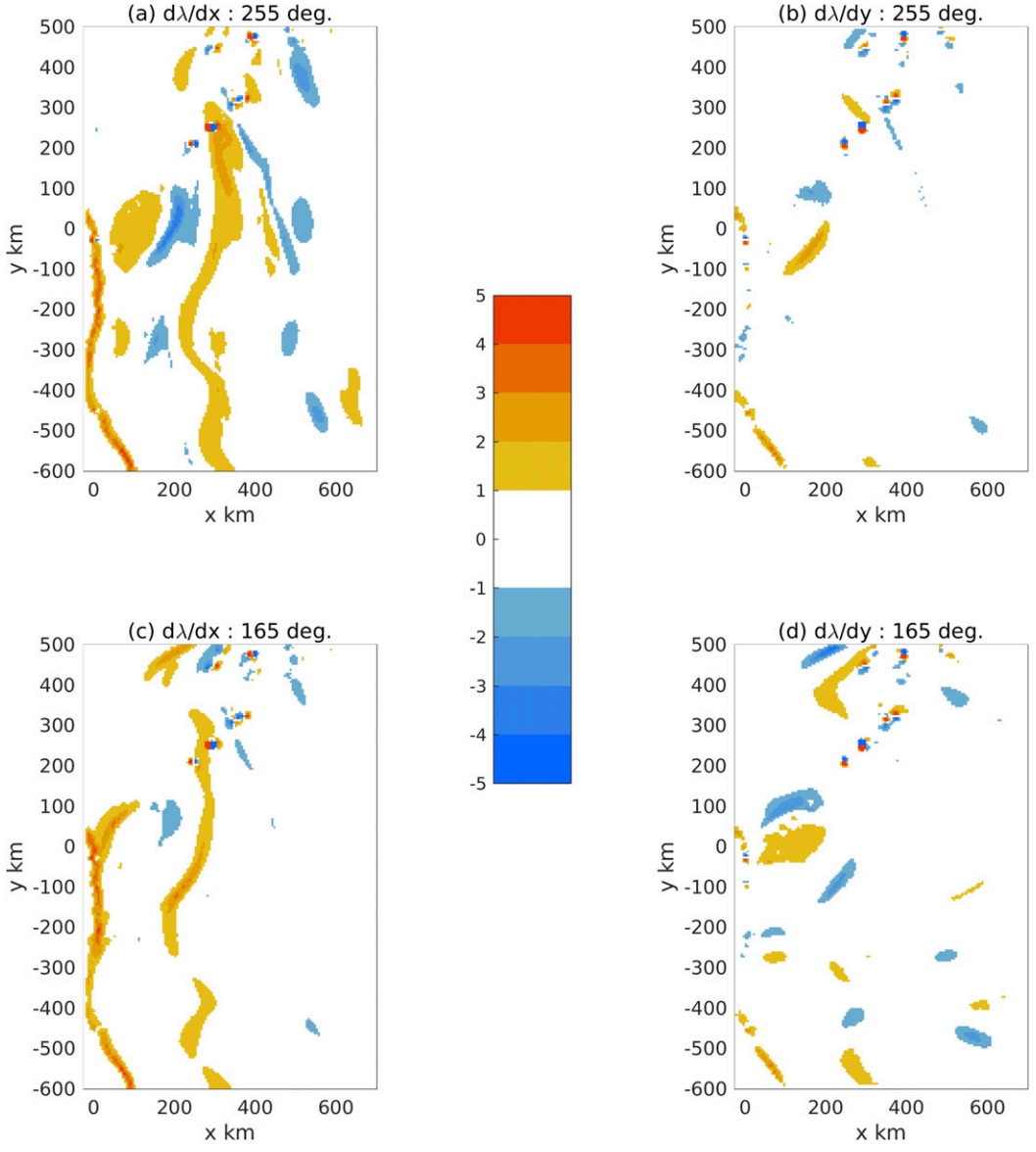

FIG. 14. The gradients $d\lambda/dx$ and $d\lambda/dy$ are plotted to evaluate whether the criterion $|d\lambda/dx| \ll 18$ is met. Gradients are plotted for the phase speeds of modes having wavenumbers in two directions, approximately (a),(b) westward (255°) and (c),(d) southward (165°). Here, coordinate x is southward at heading 165°, and y is at heading 75°. The lines of high gradient at the lower left of (a) and (c) mark the south edge of Georges Bank.

Note that long-range ray calculations of the type shown in Fig. 15 must include a curvature term to satisfy the constraint that the rays remain on the geoid; in other words, for an ocean of no current, uniform stratification, and uniform depth, modal ray trajectories would lie near geodesics, departing due to the beta effect (Zhao et al. 2018). It has been shown that propagating wave ray trajectories on the Earth can be computed by separately computing the angular deviation due to the geoid constraint and the angular deviation due to media effects (Heaney et al. 1991). For an ellipsoidal geoid such as World Geodetic System 1984 (WGS84), the polar and equatorial radii r_p and $r_{\rm eq}$ and the eccentricity $\varepsilon = (1 - r_p^2/r_{\rm eq}^2)^{1/2}$ are sufficient to determine the geodesic angular deflection per unit distance along a computed trajectory

$$\frac{d\alpha}{ds} = \frac{\sin\alpha_g}{v(\phi)}\tan\phi, \tag{8}$$

where $v(\phi) = r_{\rm eq}\,(1 - \varepsilon^2 \sin^2\phi)^{-1/2}$, α_g is ray trajectory angle clockwise from north, and ϕ is latitude. Resolution

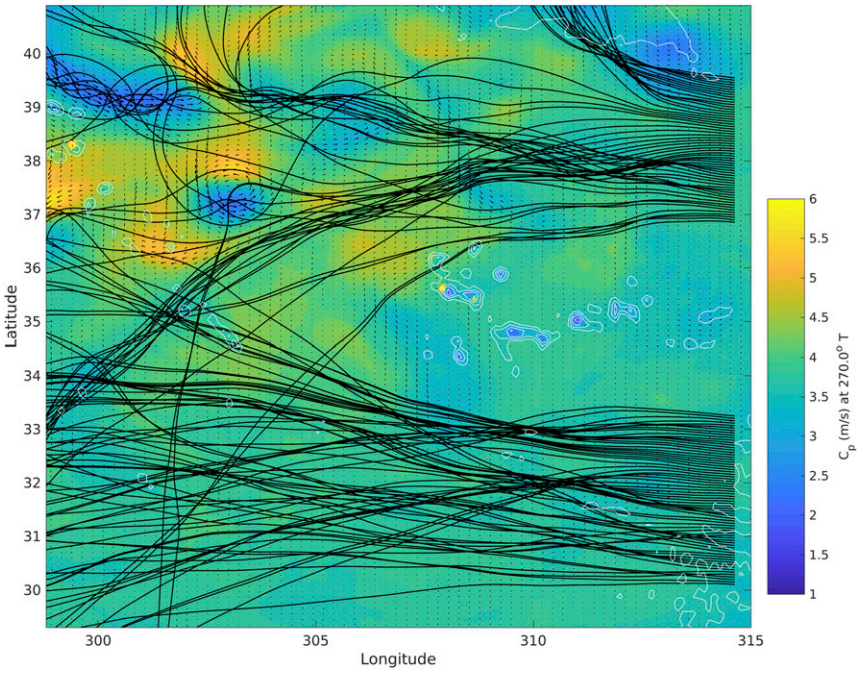

FIG. 15. Full-mode M_2 mode-one ray trajectories directed westward are shown in a large domain. The mode-one phase speed for westward wavenumber is plotted in color, and 1000, 2000, 3000, and 4000 m isobaths are shown. The Gulf Stream area is at the upper left. Rays are not plotted for the central latitudes where the Corner Seamounts cause high gradients of modal wavenumber and the eikonal equation is less accurate. Rays in the southern area where there are small gradients of the mode phase velocity do not refract as much as the rays directed southward from the Gulf of Maine. Trapping in the Gulf Stream is seen at the upper left. A caustic is seen at the upper right. The southward curvature of the ray paths caused by Earth curvature is not noticeable in the presence of the refractive effects of medium variations.

of this into coordinates and inserting the appropriate terms into the ray equations [(5)] allows the deflection because of the geoid constraint to be approximated. The beta effect is properly handled if the full modes are employed and local f is used everywhere.

f. Higher-order modal rays

Figure 16 shows rays of modes one, two, and three that move southward and eastward from the eastern Gulf of Maine radiation site to behave similarly to one another. Here, one-half as many rays are plotted for the eastern flux beam as are shown in Fig. 6a. Mode-one rays that travel southward are less likely to be trapped in the Gulf Stream and move upstream than mode-two and mode-three rays. Mode-three rays are the most likely to be trapped.

g. Relation of variable ray paths to spectral spreading of internal tide energy

In a steady-state system, internal tidal modal waves analyzed for a single tidal constituent from fixed generation sites tied to the seabed, as done here, will have constant frequency in the Eulerian reference frame. Wave fields associated with crossing and interfering waves (rays) of one frequency will have waveforms of that frequency. Thus, incoherence of internal tides does not stem solely from the processes examined here. However, it is easy to show that a sum of fixed-ray-path waves of identical frequency at generation, each with time-dependent amplitudes, will create phase shifts and departure of the resultant waveform from the generation frequency. Evolving multiple ray paths adding to form a resultant internal tide phasor will also exhibit phase wander, that is, an incoherent internal tide. Internal tides in evolving background conditions causing ray-origin changes (moving generation sites) could be modeled with amplitude dependence of fixed-path rays: energy from some rays will fade as energy from others grows, simulating the generation-site movement. This process will lead to wandering phase of internal tidal waveforms measured in the Eulerian frame and can be modeled with rays if desired, despite the fact that frequency is preserved as modal waves propagate along ray paths.

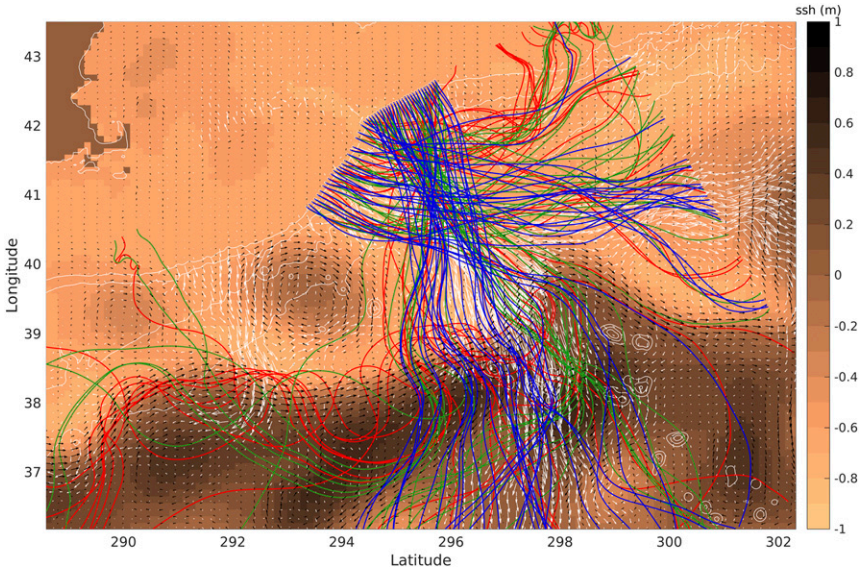

FIG. 16. The M_2 ray trajectories of the eastern beam computed using full modes for one time snapshot are plotted. Rays for modes one, two, and three are colored blue, green, and red, respectively. Bathymetry is contoured at 0, 1000, 2000, 3000, and 4000 m. Internal tidal energy fluxes from 4-km HYCOM for 1 Jul are shown in white. Surface current vectors are shown in black (1–2 Jul time period). SSH is contoured in color (1–2 Jul time period).

7. Summary and conclusions

The propagation of low-mode internal tides in the ocean is an intricate wave propagation problem. Studies of internal tide propagation made with computational hydrodynamic models have uncovered behavior such as time dependence of wave phase in eddy fields (decorrelation) (Zaron and Egbert 2014; Buijsman et al. 2017; Dunphy et al. 2017). However, clear physical explanations of the behavior can be difficult to tease out of the model fields. Here, we have used internal tidal modal ray trajectory solutions to investigate refraction of internal tides in barotropic currents. Modal properties of internal waves in baroclinic currents with rotation and background currents have been examined in detail, and modal-ray trajectories in baroclinic currents have been examined for the first time. In particular, behavior in Gulf Stream currents is considered. The motivation for choosing the Gulf Stream is that fields from a global ocean dynamical (computational) model show veering internal tide energy fluxes in this area, suggesting refraction. The strong refractive nature of modeled ray trajectories in the Gulf Stream shows how the strong azimuthal variations of mode properties in baroclinic currents cause that behavior.

One important finding is that propagating internal tide modes are subject to very strong refraction in typical meandering western boundary current baroclinic currents. In fact, it is found that few rays (i.e., little energy) will cross a current jet of this type. This results from analysis of semidiurnal fields extracted from realistically forced global HYCOM simulations, and analysis of ray trajectories predicted using subtidal (background) fields extracted from the same simulations. The ray result strictly applies to adiabatic mode propagation, where mode coupling is not considered, but the ray-path behaviors such as refraction should also hold true for the uncoupled energy fraction of a particular mode in the situation of mode coupling, where the coupling would act to drain energy from the mode under analysis. Another finding is that internal tidal modes are subject to trapping in the mode-speed minimum with respect to azimuth (the duct) that exists at the direction pointing upstream into the current. A third finding is that internal tide ray paths, which are illustrative of energy-flux paths for the actual internal tides, are predicted to be highly variable in time because they are highly sensitive to details of rapidly evolving oceanic flow features.

One major technical finding is that modal rays in baroclinic currents cannot be well approximated by rays traced in barotropic currents. Another is that the critical angle for semidiurnal mode-one ray trapping in an upstream direction in the Gulf Stream is approximately 50°.

Unlike normal mode sets that disregard currents and rotation, as used in internal tide studies that try to examine full internal tide solutions using coupled mode equations in 2D (e.g., Griffiths and Grimshaw 2007) and 3D (Kelly et al. 2016), which form a complete basis function set and are appropriate for constructing

solutions to the wave equation from modal components, the dynamically sensitive modes utilized here are not orthogonal, are not even unique at a given location when currents are sheared, and are not appropriate for that purpose. The modes used here are more closely tied to wave propagation behavior in variable media (i.e., strong mesoscale heterogeneity) and are well suited to internal tide propagation studies. Their use to study unimodal propagation, where effects of mode coupling are assumed to be small and are disregarded, requires assumptions that are no more restrictive than the typical local-mode and adiabatic-mode approximations (Rainville and Pinkel 2006), as long as it is recognized that reconstruction of the full multimode wavefield solution is beyond the capability of the method. Finally, note that extensions of ray methods can produce predictions for full wave fields (amplitude and phase everywhere; Porter and Bucker 1987), but these depend on the paraxial approximation of limited refraction which is not consistent with the ray trajectories found here, so these methods are not used here.

Acknowledgments. The Woods Hole authors wish to thank students Ms. Anne-Sophie Corbeau and Ms. Odile Hebert for their valuable contributions to the mode property research. The efforts of Jay Shriver of the Naval Research Laboratory at Stennis Space Center towards performing the HYCOM simulations and making them available are much appreciated. The Woods Hole research was supported by National Science Foundation Grant OCE-1060430 and by the Office of Naval Research Grants N00014-11-1-0701 and N00014-17-1-2624. The USM research was supported by ONR Grant N00014-15-1-2288 and National Science Foundation Grant OCE-1537449.

APPENDIX

Ray Equations for Two-Dimensional Waves with Anisotropic Wavenumbers

The equations governing ray trajectories with anisotropic (azimuthally dependent) wavenumbers can be derived using Fermat's Principle of Least Action and an eikonal equation. The derivation begins with the assumption of a progressive wave solution, which yields the eikonal equation. The eikonal equation relates gradients of wave phase and the local wave speed. Using the definitions of section 2, one can express a progressive modal wave of fixed frequency ω by

$$\begin{aligned}\psi_h(x,y,t) &= A(x,y)\tilde{w}(x,y)\exp(-i\omega t),\\ \tilde{w}(x,y) &= \exp[ixk(x,y)+iyl(x,y)] = \exp[i\omega\phi(x,y)]\\ &= \exp[i\omega(xS_x+yS_y)],\end{aligned} \tag{A1}$$

where wavenumber $\mathbf{k}(x, y) = (k, l)$, $S_x = k/\omega$, $S_y = l/\omega$, and slowness vector $\mathbf{S} = \mathbf{k}/\omega$. The spatial dependence of the eikonal function ϕ (units of time) is related to the medium properties via

$$\begin{aligned}p_x &= \frac{\partial\phi}{\partial x} = S_x + x\frac{\partial S_x}{\partial x} + y\frac{\partial S_y}{\partial x},\\ p_y &= \frac{\partial\phi}{\partial y} = S_y + y\frac{\partial S_y}{\partial y} + x\frac{\partial S_x}{\partial y}.\end{aligned} \tag{A2}$$

If the partial derivatives of the S components are set to zero, which is the *local mode approximation*, then the eikonal equation results:

$$p_x^2 + p_y^2 = S_x^2 + S_y^2 = S^2, \tag{A3}$$

where $S = |\mathbf{S}|$. The local mode approximation has already been invoked to justify the use of modes to study internal tide propagation, so this is not an additional restriction. The vertical-variation mode equations strictly apply only to x and y invariant situations and are extended to the noninvariant scenario through this approximation.

The sum of the contributions from all paths (the path integral) will be a sum of complex exponentials, and the sum will be zero for the majority of paths. However, subgroups of related paths surrounding a path with stationary phase (a path exhibiting an extremum of ϕ with respect to path variation δ) will give a nonzero result. This is Fermat's Principle of Least Action, which generalizes to Hamilton's Variational Principle for dynamical systems without dissipation (Saletan and Cromer 1971). Fermat's Principle is

$$0 = \delta\int\frac{d\phi}{dt}dt = \delta\int\left(p_x\frac{dx}{dt} + p_y\frac{dy}{dt}\right)dt, \tag{A4}$$

where the integration over time is made along the path taken by the energy of the wave (the ray), which is not required to be everywhere normal to the phase front defined by the momentum with components (p_x, p_y). Equivalently, one can write

$$0 = \delta\int L\,ds = \delta\int\frac{ds}{c_r}, \tag{A5}$$

where $c_r = c\cos(\alpha - \beta)$ is the projection of the wave phase velocity (in the direction normal to the phase front for waves with energy moving along the ray trajectory; Fig. A1) onto the ray-path increment ds (Uginčius 1972), but this form is not needed and is not used further.

The eikonal equation provides a constraint that facilitates finding a solution, and the equivalent extremum that is analyzed here is

$$0 = \delta \int \left\{ p_x \frac{dx}{dt} + p_y \frac{dy}{dt} - \lambda(t)[p_x^2 + p_y^2 - S^2(x, y, \theta)] \right\} dt. \tag{A6}$$

The integrand in all cases is the system Lagrangian L. The Hamiltonian H of the system is the dot product of speed and momentum (the first two terms) minus L, so that with the constraint we have $H = 1/2\lambda(p_x^2 + p_y^2 - S^2)$, where the multiplier has been adjusted by 1/2 for notation convenience later. The fact that H is conserved along energy propagation paths (ray paths), along which the action is minimized, results in the canonical equations relating H, the positions, and the momenta that can be solved to yield the paths (Saletan and Cromer 1971; Lighthill 1978)

$$\frac{dx}{d\zeta} = \frac{\partial H}{\partial p_x}, \quad \frac{dy}{d\zeta} = \frac{\partial H}{\partial p_y},$$
$$\frac{dp_x}{d\zeta} = \frac{-\partial H}{\partial x}, \quad \frac{dp_y}{d\zeta} = \frac{-\partial H}{\partial y}. \tag{A7a–A7d}$$

The independent variable ζ is required to be monotonically increasing along the paths (x, y). If λ is dimensionless then the independent variable ζ would have units of length squared over time. The relationship between ζ and the incremental distance along the ray path can be determined from these equations and is given later. Reducing the (A7) equations to a more readily usable form is now undertaken. The process requires the following rules and definitions:

- the phase front normal (propagation) direction is $\alpha = \arctan(p_y/p_x)$
- the ray angle is $\beta = \arctan(dy/dx)$
- $p_x = S(\alpha)\cos\alpha$ and $p_y = S(\alpha)\sin\alpha$
- $(1 + \tan^2\theta)^{-1/2} = \cos\theta$
- $\tan(a - b) = (\tan a - \tan b)/(1 + \tan a \tan b)$
- $S^2(\alpha) = (p_x^2 + p_y^2) = S^2(\alpha)(\cos^2\alpha + \sin^2\alpha)$ (x, y dependence suppressed).

The geometry of the problem is shown in Fig. A1.

Begin with one of the canonical equations:

$$\frac{dx}{d\zeta} = \frac{\partial H}{\partial p_x} = \lambda \left[p_x - S(\alpha) \frac{\partial S}{\partial \theta}\bigg|_{\theta=\alpha} \frac{\partial \theta}{\partial p_x}\bigg|_{\theta=\alpha} \right], \tag{A8}$$

where the angular partial derivatives are evaluated in the direction normal to isophase lines. From the definition of α, the final derivative is

$$\frac{\partial \theta}{\partial p_x}\bigg|_{\theta=\alpha} = \frac{-1}{1 + \tan^2\alpha} \frac{p_y}{p_x^2}, \tag{A9}$$

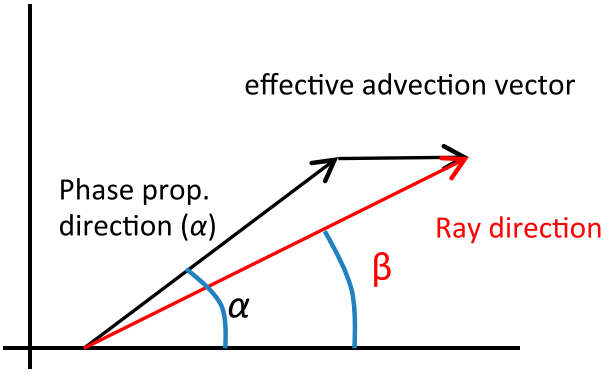

FIG. A1. The angles of the normal to the phase isolines and of the line tangent to the ray trajectory are shown, measured with respect to a baseline direction. In this example, the effect of the flow increases the group velocity in the "angle zero" direction.

so that

$$\frac{dx}{d\zeta} = \lambda \left[p_x + S(\alpha) \frac{\partial S}{\partial \theta}\bigg|_{\theta=\alpha} \frac{1}{1 + \tan^2\alpha} \frac{p_y}{p_x^2} \right]. \tag{A10}$$

Substituting for the p_x and p_y terms and converting the term with the tangent squared to $\cos^2\alpha$,

$$\frac{dx}{d\zeta} = \lambda \left[S(\alpha)\cos\alpha + \sin\alpha \frac{\partial S}{\partial \theta}\bigg|_{\theta=\alpha} \right]. \tag{A11}$$

A second canonical equation can be evaluated by noting that

$$\frac{\partial \theta}{\partial p_y}\bigg|_{\theta=\alpha} = \frac{1}{1 + \tan^2\alpha} \frac{1}{p_x}, \tag{A12}$$

which gives

$$\frac{dy}{d\zeta} = \lambda \left[S(\alpha)\sin\alpha - \cos\alpha \frac{\partial S}{\partial \theta}\bigg|_{\theta=\alpha} \right]. \tag{A13}$$

At this point the ray angle β can be determined by the two ζ derivatives,

$$\tan\beta = \frac{dy/d\zeta}{dx/d\zeta} = \frac{dy}{dx} = \frac{S(\alpha)\sin\alpha - \cos\alpha \dfrac{\partial S}{\partial \theta}\Big|_{\theta=\alpha}}{S(\alpha)\cos\alpha + \sin\alpha \dfrac{\partial S}{\partial \theta}\Big|_{\theta=\alpha}}$$
$$= \frac{S(\alpha)\tan\alpha - \dfrac{\partial S}{\partial \theta}\Big|_{\theta=\alpha}}{S(\alpha) + \tan\alpha \dfrac{\partial S}{\partial \theta}\Big|_{\theta=\alpha}}, \tag{A14}$$

from which one can evaluate the skew angle $\alpha - \beta$ (see Fig. A1; Newberry and Thompson 1989),

$$\frac{\partial S/\partial\theta|_{\theta=\alpha}}{S} = \frac{\tan\alpha - \tan\beta}{1+\tan\alpha\tan\beta} = \tan(\alpha-\beta),$$

$$\cos(\alpha-\beta) = \left[\frac{S^2(\alpha)}{S^2(\alpha)+(\partial S/\partial\theta|_{\theta=\alpha})^2}\right]^{1/2}. \quad \text{(A15)}$$

A characteristic of wave propagation is that energy travels in the direction of the group velocity, which is verified by considering the tangent of the ray angle β:

$$\tan\beta = \frac{\left[S(\alpha)\sin\alpha - \cos\alpha\left.\frac{\partial S}{\partial\theta}\right|_{\theta=\alpha}\right]\Big/\left(1-\frac{\omega}{S}\frac{\partial S}{\partial\omega}\right)}{\left[S(\alpha)\cos\alpha + \sin\alpha\left.\frac{\partial S}{\partial\theta}\right|_{\theta=\alpha}\right]\Big/\left(1-\frac{\omega}{S}\frac{\partial S}{\partial\omega}\right)} = \frac{V_{gy}}{V_{gx}}, \quad \text{(A16)}$$

where $(V_{gx}, V_{gy}) = (d\omega/dk, d\omega/dl) = (d\omega/dS\ dS/dk, d\omega/dS\ dS/dl)$ is the group velocity vector.

From the definition of the arc length increment ds along the ray, $ds = \sqrt{dx^2+dy^2}$, one can determine the derivative of the arc length s with respect to x:

$$\frac{ds}{dx} = \sqrt{1+\left(\frac{dy}{dx}\right)^2} = \sqrt{1+\left[\frac{S(\alpha)\tan\alpha - \left.\frac{\partial S}{\partial\theta}\right|_{\theta=\alpha}}{S(\alpha)+\tan\alpha\left.\frac{\partial S}{\partial\theta}\right|_{\theta=\alpha}}\right]^2}$$

$$= \frac{S(\alpha)\sqrt{1+\left[\left.\frac{\partial S}{\partial\theta}\right|_{\theta=\alpha}\Big/S(\alpha)\right]^2}}{S(\alpha)\cos\alpha + \sin\alpha\left.\frac{\partial S}{\partial\theta}\right|_{\theta=\alpha}}, \quad \text{(A17)}$$

and then write

$$\frac{ds}{dx} = \frac{S(\alpha)\sqrt{1+\tan^2(\alpha-\beta)}}{S(\alpha)\cos\alpha + \sin\alpha\left.\frac{\partial S}{\partial\theta}\right|_{\theta=\alpha}}, \quad \text{(A18)}$$

which can be modified by using the relationship of tangent to cosine, then inverted to form

$$\frac{dx}{ds} = [S(\alpha)]^{-1}\cos(\alpha-\beta)\left[S(\alpha)\cos\alpha + \sin\alpha\left.\frac{\partial S}{\partial\theta}\right|_{\theta=\alpha}\right]. \quad \text{(A19)}$$

Combining (A19) and (A11) yields

$$\frac{d\zeta}{ds} = [\lambda S(\alpha)]^{-1}\cos(\alpha-\beta). \quad \text{(A20)}$$

Thus, the independent variable ζ is the arc length projection on to the phase normal scaled by the slowness and λ to give the units of phase (time). Combining (A20) and (A13) gives

$$\frac{dy}{ds} = [S(\alpha)]^{-1}\cos(\alpha-\beta)\left[S(\alpha)\sin\alpha - \cos\alpha\left.\frac{\partial S}{\partial\theta}\right|_{\theta=\alpha}\right]. \quad \text{(A21)}$$

The third and fourth canonical equations are simpler to evaluate,

$$\frac{dp_x}{ds} = \frac{\partial p_x}{\partial\zeta}\frac{d\zeta}{ds} = \frac{-\partial H}{\partial x}\frac{d\zeta}{ds} = \cos(\alpha-\beta)\frac{\partial S}{\partial x},$$

$$\frac{dp_y}{ds} = \frac{\partial p_y}{\partial\zeta}\frac{d\zeta}{ds} = \frac{-\partial H}{\partial y}\frac{d\zeta}{ds} = \cos(\alpha-\beta)\frac{\partial S}{\partial y}, \quad \text{(A22a, A22b)}$$

providing the full set of ray trajectory equations

$$\frac{dx}{ds} = \left[S(\alpha)\cos\alpha + \sin\alpha\left.\frac{\partial S}{\partial\theta}\right|_{\theta=\alpha}\right]Q,$$

$$\frac{dy}{ds} = \left[S(\alpha)\sin\alpha - \cos\alpha\left.\frac{\partial S}{\partial\theta}\right|_{\theta=\alpha}\right]Q,$$

$$\frac{dp_x}{ds} = S(\alpha)\frac{\partial S}{\partial x}Q,$$

$$\frac{dp_y}{ds} = S(\alpha)\frac{\partial S}{\partial y}Q, \quad \text{and}$$

$$Q = [S(\alpha)]^{-1}\cos(\alpha-\beta) = \left[S^2(\alpha)+\left(\left.\frac{\partial S}{\partial\theta}\right|_{\theta=\alpha}\right)^2\right]^{-1/2}. \quad \text{(A23a–A23e)}$$

Trajectories computed with the generalized anisotropic equations [(A23)] have been compared to results obtained using Snell's law for waves in a unidirectional wind (Hohenwarter and Jelinek 2000). This is a special case of waves with anisotropic phase speed (anisotropic wavenumber), with wave speed given by the vector sum of the current and the isotropic wave speed vector in the direction normal to the phase front. The slowness vector thus contains a cosine of the wave angle, and $\partial S/\partial\theta$ has an analytical form. Figure A2 shows the comparison. The agreement is acceptable considering the very long length of the ray trace.

In the case of isotropic slowness the angular derivatives are zero, $M = \tan\alpha$, the factor $Q = S(\alpha)^{-1}$, and (A23a)–(A23d) become the standard ray equations

$$dx/ds = \cos\alpha$$
$$dy/ds = \sin\alpha$$
$$dp_x/ds = \partial S/\partial x$$
$$dp_y/ds = \partial S/\partial y. \quad \text{(A24a–A24d)}$$

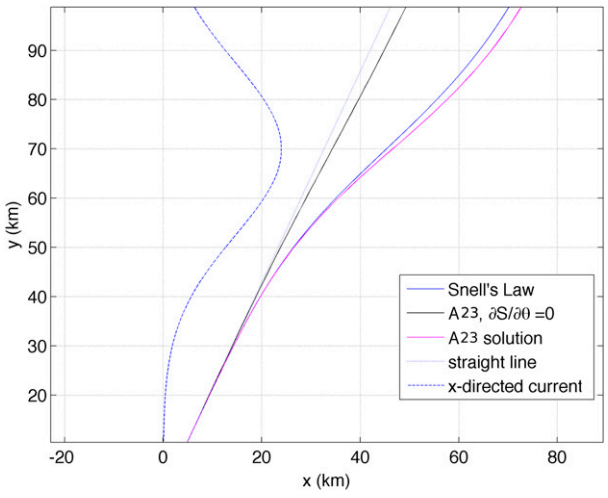

FIG. A2. The ray trajectory for a wave computed with the equations of (A23) for the case of a wave moving with a scalar wave speed and an x-directed current are compared with the solution obtained from Snell's Law, which is possible with this unidirectional current (Hohenwarter and Jelinek 2000). Here, the scalar wave speed c is 3 m s^{-1}, and the scaled and plotted x-directed advective current u has a maximum Mach number u/c of 0.4 at y = 70 km.

REFERENCES

Alford, M. H., 2003: Redistribution of energy available for ocean mixing by long-range propagation of internal waves. *Nature*, **423**, 159–162, https://doi.org/10.1038/nature01628.

——, and Z. Zhao, 2007: Global patterns of low-mode internal-wave propagation. Part II: Group velocity. *J. Phys. Oceanogr.*, **37**, 1849–1858, https://doi.org/10.1175/JPO3086.1.

Ansong, J. K., B. K. Arbic, M. C. Buijsman, J. G. Richman, J. F. Shriver, and A. J. Wallcraft, 2015: Indirect evidence for substantial damping of low-mode internal tides in the open ocean. *J. Geophys. Res. Oceans*, **120**, 6057–6071, https://doi.org/10.1002/2015JC010998.

——, and Coauthors, 2017: Semidiurnal internal tide energy fluxes and their variability in a global ocean model and moored observations. *J. Geophys. Res. Oceans*, **122**, 1882–1900, https://doi.org/10.1002/2016JC012184.

Arbic, B. K., A. J. Wallcraft, and E. J. Metzger, 2010: Concurrent simulation of the eddying general circulation and tides in a global ocean model. *Ocean Modell.*, **32**, 175–187, https://doi.org/10.1016/j.ocemod.2010.01.007.

Bleck, R., 2002: An oceanic general circulation model framed in hybrid isopycnic Cartesian coordinates. *Ocean Modell.*, **4**, 55–88, https://doi.org/10.1016/S1463-5003(01)00012-9.

Buijsman, M. C., B. K. Arbic, J. A. M. Green, R. W. Helber, J. G. Richman, J. F. Shriver, P. G. Timko, and A. J. Wallcraft, 2015: Optimizing internal wave drag in a forward barotropic model with semidiurnal tides. *Ocean Modell.*, **85**, 42–55, https://doi.org/10.1016/j.ocemod.2014.11.003.

——, and Coauthors, 2016: Impact of internal wave drag on the semidiurnal energy balance in a global ocean circulation model. *J. Phys. Oceanogr.*, **46**, 1399–1419, https://doi.org/10.1175/JPO-D-15-0074.1.

——, B. K. Arbic, J. G. Richman, J. F. Shriver, A. J. Wallcraft, and L. Zamudio, 2017: Semidiurnal internal tide incoherence in the equatorial Pacific. *J. Geophys. Res. Oceans*, **122**, 5286–5305, https://doi.org/10.1002/2016JC012590.

Červený, V., 1972: Seismic rays and ray intensities in inhomogeneous anisotropic media. *Geophys. J. Int.*, **29**, 1–13, https://doi.org/10.1111/j.1365-246X.1972.tb06147.x.

Dunphy, M., and K. G. Lamb, 2014: Focusing and vertical mode scattering of the first mode internal tide by mesoscale eddy interaction. *J. Geophys. Res. Oceans*, **119**, 523–536, https://doi.org/10.1002/2013JC009293.

——, A. L. Ponte, P. Klein, and S. Le Gentil, 2017: Low-mode internal tide propagation in a turbulent eddy field. *J. Phys. Oceanogr.*, **47**, 649–665, https://doi.org/10.1175/JPO-D-16-0099.1.

Dushaw, B. D., 2002: Mapping low-mode internal tides near Hawaii using TOPEX/POSEIDON altimeter data. *Geophys. Res. Lett.*, **29**, 1250, https://doi.org/10.1029/2001GL013944.

——, 2003: Mapping and wavenumber resolution of line-integral data for observations of low-mode internal tides. *J. Atmos. Oceanic Technol.*, **20**, 1043–1059, https://doi.org/10.1175/1458.1.

——, 2006: Mode-1 internal tides in the western North Atlantic Ocean. *Deep-Sea Res. I*, **53**, 449–473, https://doi.org/10.1016/j.dsr.2005.12.009.

——, P. F. Worcester, and M. A. Dzieciuch, 2011: On the predictability of mode-1 internal tides. *Deep-Sea Res. I*, **58**, 677–698, https://doi.org/10.1016/j.dsr.2011.04.002.

Eady, E. T., 1949: Long waves and cyclone waves. *Tellus*, **1**, 33–52, https://doi.org/10.3402/tellusa.v1i3.8507.

Egbert, G. D., A. Bennett, and M. Foreman, 1994: TOPEX/POSEIDON tides estimated using a global inverse model. *J. Geophys. Res.*, **99**, 24 821–24 852, https://doi.org/10.1029/94JC01894.

Elmore, W. C., and M. A. Heald, 1985: *Physics of Waves.* Dover, 477 pp.

Garrett, C., and E. Kunze, 2007: Internal tide generation in the deep ocean. *Annu. Rev. Fluid Mech.*, **39**, 57–87, https://doi.org/10.1146/annurev.fluid.39.050905.110227.

Gerkema, T, F.-P. A. Lam, and L. R. M. Maas, 2004: Internal tides in the Bay of Biscay: Conversion rates and seasonal effects. *Deep-Sea Res. II*, **51**, 2995–3008, https://doi.org/10.1016/j.dsr2.2004.09.012.

Griffiths, S. D., and R. H. J. Grimshaw, 2007: Internal tide generation at the continental shelf modeled using a modal decomposition: Two-dimensional results. *J. Phys. Oceanogr.*, **37**, 428–451, https://doi.org/10.1175/JPO3068.1.

Haji, M. N., 2015: Scattering of the low-mode internal tide at the Line Islands Ridge. M.S. thesis, WHOI/MIT Joint Program in Applied Ocean Science and Engineering, Massachusetts Institute of Technology, 122 pp., http://hdl.handle.net/1721.1/97852.

Heaney, K. D., W. A. Kuperman, and B. E. McDonald, 1991: Perth–Bermuda sound propagation (1960): Adiabatic mode interpretation. *J. Acoust. Soc. Amer.*, **90**, 2586–2594, https://doi.org/10.1121/1.402062.

Hogan, T. F., and Coauthors, 2014: The Navy Global Environmental Model. *Oceanography*, **27**, 116–125, https://doi.org/10.5670/oceanog.2014.73.

Hohenwarter, D., and F. Jelinek, 2000: Snell's law of refraction and sound rays for a moving medium. *Acta Acust. Acust.*, **86**, 1–14.

Holloway, P. E., E. N. Pelinovsky, T. G. Talipova, and B. Barnes, 1997: A nonlinear model of internal tide transformation on

the Australian North West Shelf. *J. Phys. Oceanogr.*, **27**, 871–896, https://doi.org/10.1175/1520-0485(1997)027<0871:ANMOIT>2.0.CO;2.

Johnston, T. M. S., and M. A. Merrifield, 2003: Internal tide scattering at seamounts, ridges, and islands. *J. Geophys. Res.*, **108**, 3180, https://doi.org/10.1029/2002JC001528.

——, ——, and P. E. Holloway, 2003: Internal tide scattering at the Line Islands Ridge. *J. Geophys. Res.*, **108**, 3365, https://doi.org/10.1029/2003JC001844.

Jones, W. L., 1967: Propagation of internal gravity waves in fluids with shear flow and rotation. *J. Fluid Mech.*, **30**, 439–448, https://doi.org/10.1017/S0022112067001521.

Kelly, S. M., and J. D. Nash, 2010: Internal-tide generation and destruction by shoaling internal tides. *Geophys. Res. Lett.*, **37**, L23611, https://doi.org/10.1029/2010GL045598.

——, and P. F. J. Lermusiaux, 2016: Internal-tide interactions with the Gulf Stream and Middle Atlantic Bight shelfbreak front. *J. Geophys. Res. Oceans*, **121**, 6271–6294, https://doi.org/10.1002/2016JC011639.

——, N. L. Jones, J. D. Nash, and A. F. Waterhouse, 2013: The geography of semidiurnal mode-1 internal-tide energy loss. *Geophys. Res. Lett.*, **40**, 4689–4693, https://doi.org/10.1002/grl.50872.

——, P. F. J. Lermusiaux, T. F. Duda, and P. J. Haley, 2016: A coupled-mode shallow water model for tidal analysis: Internal-tide reflection and refraction by the Gulf Stream. *J. Phys. Oceanogr.*, **46**, 3661–3679, https://doi.org/10.1175/JPO-D-16-0018.1.

Kerry, C. G., B. S. Powell, and G. S. Carter, 2014: The impact of subtidal circulation on internal tide generation and propagation in the Philippine Sea. *J. Phys. Oceanogr.*, **44**, 1386–1405, https://doi.org/10.1175/JPO-D-13-0142.1.

Klymak, J. M., M. H. Alford, R. Pinkel, R.-C. Lien, Y. J. Yang, and T.-Y. Tang, 2011: The breaking and scattering of the internal tide on a continental slope. *J. Phys. Oceanogr.*, **41**, 926–945, https://doi.org/10.1175/2010JPO4500.1.

Kunze, E., 2017: Internal-wave-driven mixing: Global geography and budgets. *J. Phys. Oceanogr.*, **47**, 1325–1345, https://doi.org/10.1175/JPO-D-16-0141.1.

Lamb, K., and M. Dunphy, 2016: Tide-topography interactions: Asymmetries in internal wave generation due to surface trapped currents. *Ninth Int. Symp. on Stratified Flows*, San Diego, CA, Scripps Institution of Oceanography, 6 pp., http://escholarship.org/uc/item/80h8k5hf.

Landau, L. D., and E. M. Lifshitz, 1960: *Electrodynamics of Continuous Media*. Pergamon Press, 417 pp.

Legg, S., 2014: Scattering of low-mode internal waves at finite isolated topography. *J. Phys. Oceanogr.*, **44**, 359–383, https://doi.org/10.1175/JPO-D-12-0241.1.

Li, Q., and D. M. Farmer, 2011: The generation and evolution of nonlinear internal waves in the deep basin of the South China Sea. *J. Phys. Oceanogr.*, **41**, 1345–1363, https://doi.org/10.1175/2011JPO4587.1.

Lighthill, J., 1978: *Waves in Fluids.* Cambridge University Press, 524 pp.

Mathur, M., G. S. Carter, and T. Peacock, 2014: Topographic scattering of the low-mode internal tide in the deep ocean. *J. Geophys. Res. Oceans*, **119**, 2165–2182, https://doi.org/10.1002/2013JC009152.

Milder, D. M., 1969: Ray and wave invariants for SOFAR channel propagation. *J. Acoust. Soc. Amer.*, **46**, 1259–1263, https://doi.org/10.1121/1.1911850.

Nash, J. D., S. M. Kelly, E. L. Shroyer, J. N. Moum, and T. F. Duda, 2012: The unpredictable nature of internal tides on continental shelves. *J. Phys. Oceanogr.*, **42**, 1981–2000, https://doi.org/10.1175/JPO-D-12-028.1.

Newberry, B. P., and R. B. Thompson, 1989: A paraxial theory for the propagation of ultrasonic beams in anisotropic solids. *J. Acoust. Soc. Amer.*, **85**, 2290–2300, https://doi.org/10.1121/1.397775.

Niwa, Y., and T. Hibiya, 2001: Numerical study of the spatial distribution of the M_2 internal tide in the Pacific Ocean. *J. Geophys. Res.*, **106**, 22 441–22 449, https://doi.org/10.1029/2000JC000770.

Paoletti, M. S., M. Drake, and H. L. Swinney, 2014: Internal tide generation in nonuniformly stratified deep oceans. *J. Geophys. Res. Oceans*, **119**, 1943–1956, https://doi.org/10.1002/2013JC009469.

Park, J.-H., and D. R. Watts, 2006: Internal tides in the southwestern Japan/East Sea. *J. Phys. Oceanogr.*, **36**, 22–34, https://doi.org/10.1175/JPO2846.1.

Pierce, A. D., 1965: Extension of the method of normal modes to sound propagation in an almost-stratified medium. *J. Acoust. Soc. Amer.*, **37**, 19–27, https://doi.org/10.1121/1.1909303.

Ponte, A. L., and P. Klein, 2015: Incoherent signature of internal tides on sea level in idealized numerical simulations. *Geophys. Res. Lett.*, **42**, 1520–1526, https://doi.org/10.1002/2014GL062583.

Porter, M. B., and H. P. Bucker, 1987: Gaussian beam tracing for computing ocean acoustic fields. *J. Acoust. Soc. Amer.*, **82**, 1349–1359, https://doi.org/10.1121/1.395269.

Rainville, L., and R. Pinkel, 2006: Propagation of low-mode internal waves through the ocean. *J. Phys. Oceanogr.*, **36**, 1220–1236, https://doi.org/10.1175/JPO2889.1.

——, T. M. Johnston, G. S. Carter, M. A. Merrifield, R. Pinkel, P. F. Worcester, and B. D. Dushaw, 2010: Interference pattern and propagation of the M_2 internal tide south of the Hawaiian Ridge. *J. Phys. Oceanogr.*, **40**, 311–325, https://doi.org/10.1175/2009JPO4256.1.

Ray, R. D., and G. T. Mitchum, 1996: Surface manifestation of internal tides generated near Hawaii. *Geophys. Res. Lett.*, **23**, 2101–2104, https://doi.org/10.1029/96GL02050.

——, and D. E. Cartwright, 2001: Estimates of internal tide energy fluxes from TOPEX/ POSEIDON altimetry: Central North Pacific. *Geophys. Res. Lett.*, **28**, 1259–1262, https://doi.org/10.1029/2000GL012447.

——, and E. D. Zaron, 2016: M_2 internal tides and their observed wavenumber spectra from satellite altimetry. *J. Phys. Oceanogr.*, **46**, 3–22, https://doi.org/10.1175/JPO-D-15-0065.1.

Saletan, E. J., and A. H. Cromer, 1971: *Theoretical Mechanics.* John Wiley and Sons, 376 pp.

Savage, A. C., and Coauthors, 2017: Frequency content of sea surface height variability from internal gravity waves to mesoscale eddies. *J. Geophys. Res. Oceans*, **122**, 2519–2538, https://doi.org/10.1002/2016JC012331.

Sherwin, T. J., 1988: Analysis of an internal tide observed on the Malin Shelf, north of Ireland. *J. Phys. Oceanogr.*, **18**, 1035–1050, https://doi.org/10.1175/1520-0485(1988)018<1035:AOAITO>2.0.CO;2.

Shriver, J. F., B. K. Arbic, J. G. Richman, R. D. Ray, E. J. Metzger, A. J. Wallcraft, and P. G. Timko, 2012: An evaluation of the barotropic and internal tides in a high resolution global ocean circulation model. *J. Geophys. Res.*, **117**, C10024, https://doi.org/10.1029/2012JC008170.

Tisseur, F., 2000: Backward error and condition of polynomial eigenvalue problems. *Linear Algebra Appl.*, **309**, 339–361, https://doi.org/10.1016/S0024-3795(99)00063-4.

Uginčius, P., 1972: Ray acoustics and Fermat's Principle in a moving inhomogeneous medium. *J. Acoust. Soc. Amer.*, **51**, 1759–1763, https://doi.org/10.1121/1.1913024.

Vavryčuk, V., 2006: Calculation of the slowness vector from the ray vector in anisotropic media. *Proc. Roy. Soc. London*, **462A**, 883–896, https://doi.org/10.1098/rspa.2005.1605.

Vlasenko, V., N. Staschuk, and K. Hutter, 2005: *Baroclinic Tides, Theoretical Modeling and Observational Evidence.* Cambridge University Press, 351 pp.

Warn-Varnas, A., J. Hawkins, K. G. Lamb, S. Piacsek, S. Chin-Bing, D. King, and G. Burgos, 2010: Solitary wave generation dynamics at Luzon Strait. *Ocean Modell.*, **31**, 9–27, https://doi.org/10.1016/j.ocemod.2009.08.002.

Wunsch, C., and R. Ferrari, 2004: Vertical mixing, energy, and the general circulation of the oceans. *Annu. Rev. Fluid Mech.*, **36**, 281–314, https://doi.org/10.1146/annurev.fluid.36.050802.122121.

Zaron, E. D., and G. D. Egbert, 2014: Time-variable refraction of the internal tide at the Hawaiian Ridge. *J. Phys. Oceanogr.*, **44**, 538–557, https://doi.org/10.1175/JPO-D-12-0238.1.

Zhang, H. P., B. King, and H. L. Swinney, 2008: Resonant generation of internal waves on a model continental slope. *Phys. Rev. Lett.*, **100**, 244504, https://doi.org/10.1103/PhysRevLett.100.244504.

Zhang, L., and H. L. Swinney, 2014: Virtual seafloor reduces internal wave generation by tidal flow. *Phys. Rev. Lett.*, **112**, 104502, https://doi.org/10.1103/PhysRevLett.112.104502.

——, M. C. Buijsman, E. Comino, and H. L. Swinney, 2017: Internal wave generation by tidal flow over periodically and randomly distributed seamounts. *J. Geophys. Res. Oceans*, **122**, 5063–5074, https://doi.org/10.1002/2017JC012884.

Zhang, W. G., and T. F. Duda, 2013: Intrinsic nonlinearity and spectral structure of internal tides at an idealized Mid-Atlantic Bight Shelfbreak. *J. Phys. Oceanogr.*, **43**, 2641–2660, https://doi.org/10.1175/JPO-D-12-0239.1.

——, ——, and I. A. Udovydchenkov, 2014: Modeling and analysis of internal-tide generation and beamlike onshore propagation in the vicinity of shelfbreak canyons. *J. Phys. Oceanogr.*, **44**, 834–849, https://doi.org/10.1175/JPO-D-13-0179.1.

Zhao, Z., and M. H. Alford, 2009: New altimetric estimates of mode-one M_2 internal tides in the central North Pacific Ocean. *J. Phys. Oceanogr.*, **39**, 1669–1684, https://doi.org/10.1175/2009JPO3922.1.

——, ——, J. A. MacKinnon, and R. Pinkel, 2010: Long-range propagation of the semidiurnal internal tides from the Hawaiian Ridge. *J. Phys. Oceanogr.*, **40**, 713–736, https://doi.org/10.1175/2009JPO4207.1.

——, ——, J. Girton, T. M. S. Johnston, and G. Carter, 2011: Internal tides around the Hawaiian Ridge estimated from multisatellite altimetry. *J. Geophys. Res.*, **116**, C12039, https://doi.org/10.1029/2011JC007045.

——, ——, ——, L. Rainville, and H. L. Simmons, 2016: Global observations of open-ocean mode-1 M_2 internal tides. *J. Phys. Oceanogr.*, **46**, 1657–1684, https://doi.org/10.1175/JPO-D-15-0105.1.

——, ——, H. L. Simmons, D. Brazhnikov, and R. Pinkel, 2018: Satellite investigation of the M_2 internal tide in the Tasman Sea. *J. Phys. Oceanogr.*, **48**, 687–703, https://doi.org/10.1175/JPO-D-17-0047.1.